


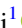


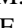





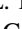
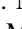



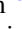






# PALFA Single-pulse Pipeline: New Pulsars, Rotating Radio Transients, and a Candidate Fast Radio Burst

C. Patel<sup>1</sup>, D. Agarwal<sup>2,3</sup>, M. Bhardwaj<sup>1</sup> , M. M. Boyce<sup>1</sup>, A. Brazier<sup>4,5,6</sup>, S. Chatterjee<sup>7</sup> , P. Chawla<sup>1</sup> , V. M. Kaspi<sup>1</sup> ,  
D. R. Lorimer<sup>2,3</sup> , M. A. McLaughlin<sup>2,3</sup> , E. Parent<sup>1</sup> , Z. Pleunis<sup>1</sup> , S. M. Ransom<sup>8</sup> , P. Scholz<sup>9</sup> , R. S. Wharton<sup>10</sup> ,  
W. W. Zhu<sup>10,11,12</sup> , M. Alam<sup>13</sup>, K. Caballero Valdez<sup>14</sup>, F. Camilo<sup>15</sup> , J. M. Cordes<sup>7</sup> , F. Crawford<sup>13</sup> , J. S. Deneva<sup>16</sup> ,  
R. D. Ferdman<sup>17</sup> , P. C. C. Freire<sup>10</sup> , J. W. T. Hessels<sup>18,19</sup>, B. Nguyen<sup>13</sup>, I. Stairs<sup>20</sup> , K. Stovall<sup>21</sup> , and J. van Leeuwen<sup>18,19</sup>

<sup>1</sup> Department of Physics and McGill Space Institute, McGill University, Montreal, QC H3A 2T8, Canada

<sup>2</sup> Department of Physics and Astronomy, West Virginia University, Morgantown, WV 26506, USA

<sup>3</sup> Center for Gravitational Waves and Cosmology, West Virginia University, Chestnut Ridge Research Building, Morgantown, WV 26506, USA

<sup>4</sup> Department of Astronomy, Cornell Center for Astrophysics and Space Science, Space Science Building, Ithaca, NY 14853, USA

<sup>5</sup> Cornell Center for Advanced Computing, Frank H. T. Rhodes Hall, Hoy Road, Ithaca, NY 14853, USA

<sup>6</sup> Department of Astronomy, Cornell University, Ithaca, NY 14853, USA

<sup>7</sup> Cornell Center for Astrophysics and Planetary Science and Department of Astronomy, Cornell University, Ithaca, NY 14853, USA

<sup>8</sup> National Radio Astronomy Observatory, Charlottesville, VA 22903, USA

<sup>9</sup> National Research Council of Canada, Herzberg Astronomy and Astrophysics, Dominion Radio Astrophysical Observatory, P.O. Box 248, Penticton, BC V2A 6J9, Canada

<sup>10</sup> Max-Planck-Institut für Radioastronomie, Auf dem Hügel 69, D-53121 Bonn, Germany

<sup>11</sup> National Astronomical Observatories, Chinese Academy of Science, 20A Datun Road, Chaoyang District, Beijing 100012, People's Republic of China

<sup>12</sup> CAS Key Laboratory of FAST, NAOC, Chinese Academy of Science, 20A Datun Road, Chaoyang District, Beijing 100012, People's Republic of China

<sup>13</sup> Department of Physics and Astronomy, Franklin and Marshall College, Lancaster, PA 17604-3003, USA

<sup>14</sup> University of Texas Rio Grande Valley, 1 West University Boulevard, Brownsville, TX 78520, USA

<sup>15</sup> South African Radio Astronomy Observatory (SARAO), Cape Town, 7925, South Africa

<sup>16</sup> George Mason University, resident at the Naval Research Laboratory, Washington, DC 20375, USA

<sup>17</sup> Faculty of Science, University of East Anglia, Norwich Research Park, Norwich NR4 7TJ, UK

<sup>18</sup> ASTRON, The Netherlands Institute for Radio Astronomy, Postbus 2, 7990 AA, Dwingeloo, The Netherlands

<sup>19</sup> Anton Pannekoek Institute for Astronomy, University of Amsterdam, Science Park 904, 1098 XH Amsterdam, The Netherlands

<sup>20</sup> Department of Physics and Astronomy, University of British Columbia, Vancouver, BC V6T 1Z1, Canada

<sup>21</sup> National Radio Astronomy Observatory, P.O. Box 0, Socorro, NM 87801, USA

Received 2018 August 16; revised 2018 October 21; accepted 2018 October 31; published 2018 December 26

## Abstract

We present a new single-pulse pipeline for the PALFA survey to efficiently identify single radio pulses from pulsars, rotating radio transients (RRATs), and fast radio bursts (FRBs). We conducted a sensitivity analysis of this new pipeline in which many single pulses were injected into PALFA data and run through the pipeline. We find that for single pulse widths  $< 5$  ms, the sensitivity of our new pipeline is at most a factor of  $\sim 2$  less sensitive than theoretically predicted. For pulse widths  $> 10$  ms, as the DM decreases, the degradation in sensitivity gets worse and can increase up to a factor of  $\sim 4.5$ . Using this pipeline, we have discovered seven pulsars and two RRATs, and identified three candidate RRATs and one candidate FRB. The confirmed pulsars and RRATs have DMs ranging from 133 to 386 pc cm<sup>-3</sup> and flux densities ranging from 20 to 160 mJy. The pulsar periods range from 0.4 to 2.1 s. We report on candidate FRB 141113, which is likely astrophysical and extragalactic, having DM  $\simeq 400$  pc cm<sup>-3</sup>, which is over the Galactic maximum along this line of sight by  $\sim 100$ –200 pc cm<sup>-3</sup>. We consider implications for the FRB population and show via simulations that if FRB 141113 is real and extragalactic, the slope  $\alpha$  of the distribution of integral source counts as a function of flux density ( $N(>S) \propto S^{-\alpha}$ ) is  $1.4 \pm 0.5$  (95% confidence range). However, this conclusion is dependent on assumptions that require verification.

*Key words:* methods: data analysis – pulsars: general

## 1. Introduction

Pulsars are rapidly rotating, highly magnetized neutron stars (NSs). The majority of currently known pulsars are best detected through their time-averaged emission. Pulsar surveys like the PALFA survey (Pulsar Arecibo L-band Feed Array; Cordes et al. 2006) generally use fast Fourier transform (FFT) searches in the frequency domain to search for pulsars. However, radio pulsar surveys often suffer from the presence of red noise generated by receiver gain instabilities and terrestrial interference. This can reduce sensitivity, particularly to long-period pulsars. For example, Lazarus et al. (2015) reported that due to the presence of red noise, the sensitivity of the PALFA survey is significantly degraded for periods  $P > 0.5$  s, with a greater degradation in sensitivity for longer spin periods. In order to mitigate such problems, more effective time domain searches

like the fast-folding algorithm (FFA, see Lorimer & Kramer 2005; Kondratiev et al. 2009; Parent et al. 2018, and references therein) and single-pulse search techniques (as described by Cordes & McLaughlin 2003) can be used.

Rotating radio transients (RRATs) are a relatively recently discovered class of NSs that were detected only through their individual pulses (McLaughlin et al. 2006). Due to the sporadic nature of their emission, surveys cannot rely on standard FFT searches to effectively look for RRAT signals. Instead, single-pulse search techniques are required.

Fast radio bursts (FRBs) are also a recently discovered phenomenon characterized by short (few ms) radio bursts with high dispersion measures (DMs; Lorimer et al. 2007). Unlike RRATs, which have observed DMs smaller than the maximum Galactic DM along the line of sight as predicted by Galactic

free electron density models (Cordes & Lazio 2003; Yao et al. 2017), FRBs have DMs that are much larger than this, implying extragalactic or even cosmological distances. To date, 34 FRBs have been discovered,<sup>22</sup> with only one FRB seen to repeat (Spitler et al. 2016). Like RRATs, FRBs can only be detected via single-pulse search techniques due to their transient nature.

It is important to understand a survey’s sensitivity to FRBs and RRATs as a function of various parameters (such as pulse width, DM, scattering measure) if one is to accurately characterize the underlying sky event rates of these sources for population studies.

The PALFA survey is the most sensitive wide-area survey for radio pulsars and short radio transients ever conducted. Operating at a radio frequency band centered at 1.4 GHz, PALFA searches the Galactic plane ( $|b| < 5^\circ$ ), using the Arecibo Observatory, the 305 m single dish radio telescope located in Arecibo, Puerto Rico (see Cordes et al. 2006; Deneva et al. 2009; Lazarus et al. 2015, for more details). Since the survey began in 2004, it has discovered 178 pulsars, including 15 RRATs and one FRB. Lazarus et al. (2015) comprehensively characterized the sensitivity of PALFA to radio pulsars, and showed that it is sensitive to millisecond pulsars as predicted by theoretical models based on the radiometer equation, which assumes white noise. However, PALFA suffers significant degradation to long-period pulsars due to the presence of red noise in the data. In order to improve the search for long-period pulsars, the PALFA collaboration has introduced a fast-folding algorithm (Parent et al. 2018).

Deneva et al. (2009) described an early single-pulse search algorithm for PALFA, reporting on the discovery of seven objects. Here, we describe a new single-pulse search pipeline that we have also introduced to help identify long-period pulsars, RRATs, and FRBs in our data. This new pipeline is described in Section 2. In Section 3, we describe the survey’s sensitivity to single pulses using an injection analysis. In Section 4, we report new and candidate astrophysical sources discovered by this pipeline. In Section 5, we compare the number of RRATs detected by our survey with the predicted number from population synthesis of RRATs in the PALFA survey. We discuss a new candidate FRB, FRB 141113, in Section 6, and its implications for the FRB population in Section 7. We present our conclusions in Section 8.

## 2. The Single-pulse Pipeline

### 2.1. Overview of the Pipeline

The PALFA survey uses a pipeline based on the software package PRESTO (Ransom 2001) to search the observations for pulsars and radio transients. The processing is done on the Guillimin supercomputer, which is the property of Compute Canada/Calcul Quebec, operated by McGill University’s High Performance Computing Centre.<sup>23</sup>

The data management, preprocessing of the data, radio frequency interference (RFI) mitigation, dedispersion, and single-pulse search techniques used by the PALFA consortium have been explained in detail by Deneva et al. (2009) and Lazarus et al. (2015). Indeed, single-pulse searching has been a part of the pipeline since 2011. However, as described in this paper, the PALFA consortium has now implemented a more robust single-

pulse pipeline in 2015 July. This required adding more systematic and automated removal of radio frequency interference (RFI), as well as more automated candidate identification and visualization postprocessing tools. After single-pulse searching using the standard PRESTO `single_pulse_search.py` routine, the pipeline now makes use of a clustering algorithm to group single-pulse events and rank them (see Section 2.2) according to a well-defined metric to classify pulsar, RRAT, and FRB (henceforth “astrophysical”) candidates. A final diagnostic plot is produced for each candidate selected by the grouping algorithm so that it can be viewed by the members of the PALFA consortium to decide whether the candidate is astrophysical (see Section 2.3 for more details). To aid in verifying astrophysical candidates, we introduced a series of heuristic ratings (Section 2.4) and a machine-learning algorithm (Section 2.5) that is applied to each candidate. The candidates are viewed via an online collaborative facility, CyberSKA<sup>24</sup> (Kiddle et al. 2011 Section 2.6).

### 2.2. Grouping and Ranking of Single Pulses

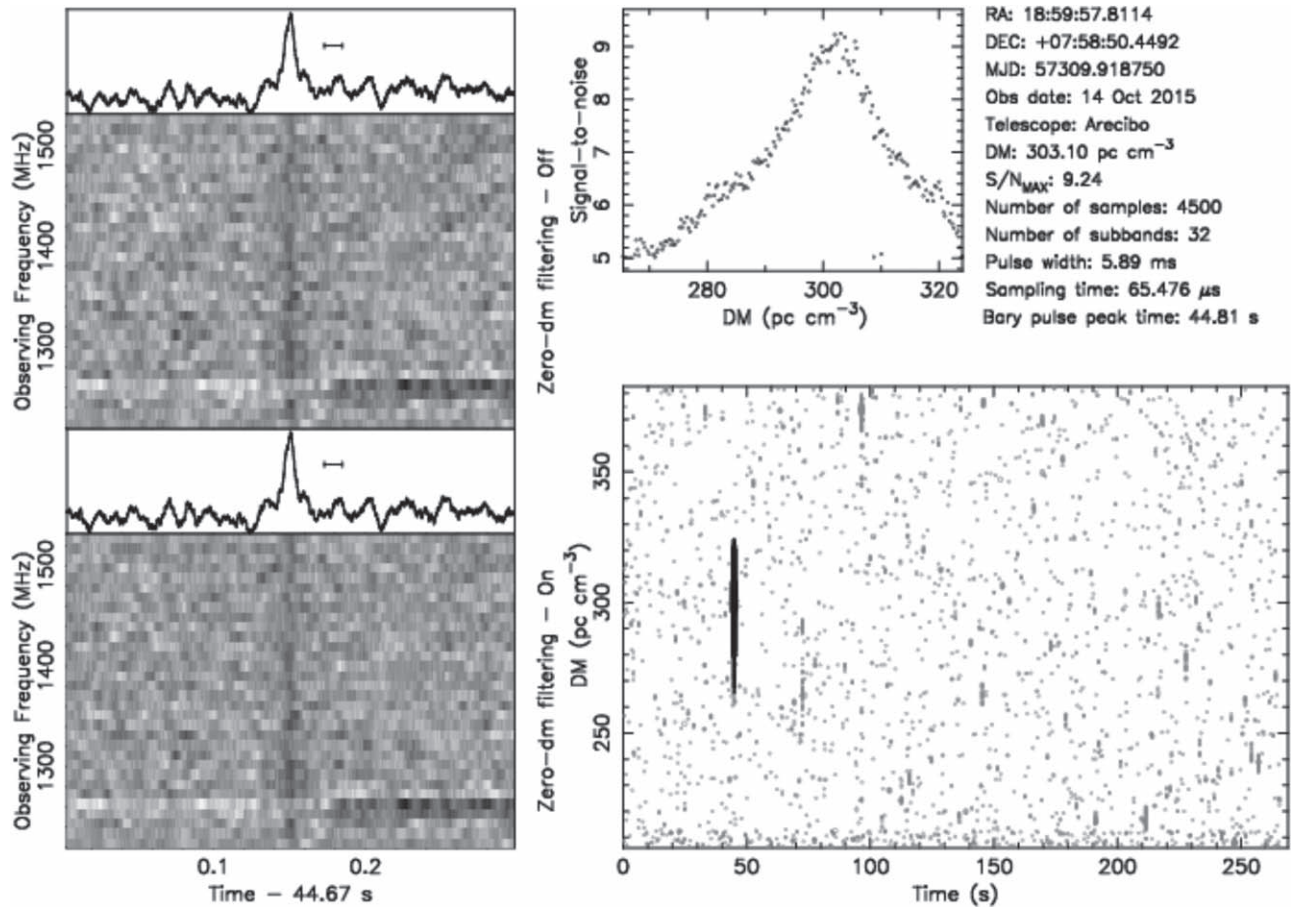
After the single-pulse search has been conducted on each time series, the output is sifted by the grouping algorithm RRATtrap (Karako-Argaman et al. 2015), which clusters nearby single-pulse events into separate groups based on relative proximity in time and DM. The grouped pulses are then ranked based on the criterion that the signal-to-noise ratio (S/N) of astrophysical pulses peaks at the optimal DM and falls off on either side (see the top right plot in Figure 1). The RRATtrap algorithm was further improved and adapted for the PALFA survey as follows:

1. The relative proximity in DM and time between single-pulse events that is required to cluster them into a single group is now dependent on the DM, instead of being fixed. The dependence is dictated by the dedispersion plan for the survey, described in Lazarus et al. (2015), with the grouping threshold in DM and time being multiples of the corresponding DM step size and downsampling factor, respectively.
2. The minimum group size required for a cluster to be considered a signal is no longer a fixed number but based on the expected S/N-DM curve (Equations (12) and (13) of Cordes & McLaughlin 2003 and Equation (1), provided later), given the observed S/N and pulse width. If the actual group size is smaller than the estimated one, the event is deemed to be noise.
3. If an astrophysical pulse is very narrow, it should only be detectable in a few neighboring DMs, with the number depending on the DM spacing. This results in a group size that is well below the minimum described previously. In order to avoid missing these candidates, we created a new classification criterion. If the maximum S/N in the group of events is greater than 10, even if there are very few pulses ( $< 20$ ), for a small pulse width ( $< 5$  ms) and a high DM ( $DM > 500 \text{ pc cm}^{-3}$ ), this group is classified as astrophysical and is subject to further investigation by the pipeline.
4. Pulses generated by narrow-band RFI tend to span a large DM range, but bright astrophysical pulses could also form groups that span large DM ranges. Instead of having a fixed number for a maximum allowed DM span as described by Karako-Argaman et al. (2015), we now

<sup>22</sup> [www.frbcat.org](http://www.frbcat.org)

<sup>23</sup> <http://www.hpc.mcgill.ca/>

<sup>24</sup> [www.cyberska.org](http://www.cyberska.org)



**Figure 1.** “Spd” plot for RRAT J1859+07. Left dedispersed frequency vs. time plots (dynamic spectra). The dedispersed time series are shown as line plots in the panels above the dedispersed frequency vs. time grayscale plots, produced by summing the frequency channels below. The top plot is produced without zero-DM filtering, while the bottom plot uses a zero-DM filter (Eatough et al. 2009). Top right: S/N vs. DM of the black pulse in the bottom right window, showing that the S/N peaks near the optimal DM and decreases away from it. Bottom right: DM vs. time for all single pulse events detected by PRESTO’s `single_pulse_search.py`. The higher the S/N of the event, the bigger the size of the point in the plot. The pulse in black is the candidate for which frequency vs. time and S/N vs. DM sub-plots are generated. Relevant header information about the candidate is displayed on the top right. See Section 2.3 for details.

estimate the DM range an astrophysical pulse should be detected over for a given S/N at the optimal DM, as described by Cordes & McLaughlin (2003). If the group spans a DM range greater than a factor of five times our estimate, it is classified as RFI.

### 2.3. Production of the Single-pulse Candidates

In order to make the search process more efficient and systematic, all candidates classified as being astrophysical by the grouping algorithm (Section 2.2) undergo automatic production of single-pulse diagnostic (“spd”) plots to help with human verification. The spd plots contain all the features necessary to verify whether the candidate is astrophysical or is RFI. An example of such a plot is shown in Figure 1 for RRAT J1859+07.

On average, 20 such candidates are produced per beam. There is a binary output file produced for each candidate that can be used to reproduce the plot. These candidates are subject to a variety of heuristic ratings (see Section 2.4) and exposed to a machine-learning algorithm that also rates them (Section 2.5). They are then uploaded to a database at the Center for Advanced Computing (CAC), located at Cornell University,

and can be viewed on our online candidate viewer (see Section 2.6).

### 2.4. Ratings

Currently, 10 heuristic ratings are applied to each single-pulse candidate produced by the pipeline, assessing different properties of the signal. The different ratings are described in Table 1. In the pipeline, they are applied to the candidate spd files. They assist the viewers in differentiating potential astrophysical candidates from RFI.

### 2.5. Machine-learning Candidate Selection

The single-pulse candidates produced by the pipeline are also exposed to a machine-learning algorithm that attempts to select astrophysical candidates. The single-pulse pipeline uses the same machine-learning algorithm as employed by the periodicity pipeline and explained by Zhu et al. (2014). It uses an image pattern recognition system that mimics humans to distinguish pulsar signals from noise/RFI candidates. The algorithm is trained regularly based on the manual classification of candidates by members of the collaboration. Since the algorithm was designed to view the periodicity candidate plots,

**Table 1**  
Heuristic Single-pulse Candidate Ratings

Ratings	Description
Peak Over rms	The ratio of the peak amplitude of the profile to the rms amplitude
Phase Consistency	The fraction of sub-bands that are in-phase in the pulse window by $\leq 2\%$ . The offset is calculated by cross-correlating each interval with the summed profile.
Gaussian Amplitude	The amplitude of a single-Gaussian fit to the profile, normalized such that the profile standard deviation is 1
Gaussian Goodness	The reduced $\chi^2$ of a single-Gaussian fit to the profile
Gaussian FWHM	The full width at half maximum of a single-Gaussian fit to the profile
Fraction of Good Sub-bands	The fraction of frequency sub-bands above a set S/N threshold that contain the signal
Sub-band S/N Standard Deviation	The standard deviation of the sub-band S/N ratios
Known Pulsar Rating	The similarity of the position and DM to those of a known pulsar. The value is between 0 and 1, with values closer to 1 indicating similarity to a known pulsar.
Maximum DM Ratio	The ratio of the candidate DM to the maximum Galactic DM in the candidate direction, according to the NE2001 electron density model (Cordes & Lazio 2003).

slight changes were made for it to work on the single-pulse “spd” candidate plots (Figure 1):

1. The zero-DM filtered, dedispersed time series of the “spd” plot replaces the pulse profile of a periodicity candidate
2. The zero-DM filtered, dedispersed dynamic spectrum of the “spd” plot acts like time versus phase and frequency versus phase sub-plot of a periodicity candidate
3. The dynamic spectrum of the “spd” plot is dedispersed for a range of DMs around the best DM, and a time series is produced for each DM trial. The time series for each DM is analyzed and a plot of reduced  $\chi^2$  versus DM (similar to that of a periodicity candidate) is produced for the machine-learning algorithm to analyze.

### 2.6. Candidate Viewer: CyberSKA

All the candidates produced by our pipeline are uploaded to the results database at CAC. The results can be viewed online via the CyberSKA portal (Kiddle et al. 2011). The PALFA collaboration has developed several applications on this portal for viewing periodicity search candidates (Lazarus et al. 2015). We developed a new application for viewing single-pulse candidates that is very similar to the existing application. Specifically, we can filter using queries on different candidate properties, ratings (Section 2.4), and file metadata information. As with our periodicity candidate viewer, single-pulse candidates can be classified as astrophysical, RFI, noise, or known sources. The best candidates are uploaded to a Top Candidates database and are eventually followed up for confirmation.

## 3. Survey Sensitivity to Single Pulses

The peak flux densities of single pulses are generally estimated using the following equation from Cordes & McLaughlin (2003):

$$S_i = \frac{\beta(S/N)_b(T_{\text{sys}} + T_{\text{sky}})}{GW_i} \sqrt{\frac{W_b}{n_p \Delta f}}, \quad (1)$$

where  $S_i$  is the intrinsic flux density;  $\beta$  is a factor accounting for the sensitivity loss due to digitization;  $(S/N)_b$  is the S/N of the broadened pulse;  $T_{\text{sys}}$  and  $T_{\text{sky}}$  are the system temperature at the observing frequency and the sky temperature, respectively;  $G$  is

**Table 2**  
Injected Pulse Parameters<sup>a</sup>

Parameter	Values
Pulse Width (ms)	0.99, 2.04, 5, 10.1, 20.03
DM (pc cm <sup>-3</sup> )	42.5, 153.7, 326.2, 615.5 1005.7, 5606.7
Scattering Time (ms)	0
Pulse Width (ms)	~5
DM (pc cm <sup>-3</sup> )	1005.7
Scattering Time (ms)	10, 20, 50, 100

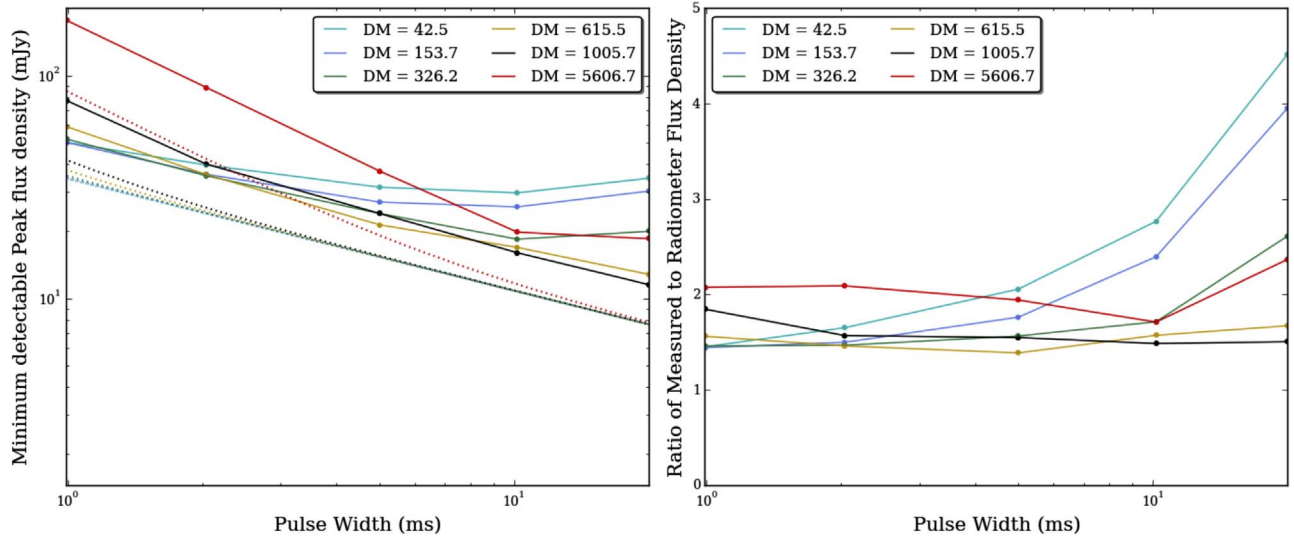
**Note.**

<sup>a</sup> The upper panel shows the injection parameters used for the analysis done in absence of pulse broadening due to scattering, while the lower panel shows the parameters used for the analysis when accounting for pulse broadening due to scattering.

the telescope gain;  $W_i$  and  $W_b$  are the intrinsic and broadened pulse widths, respectively;  $n_p$  is the number of summed polarizations; and  $\Delta f$  is the observing bandwidth. Equation (1) is a theoretical representation of the sensitivity to single pulses in the presence of Gaussian noise. The sensitivity to single pulses in real survey data (which contains RFI and other non-Gaussian features) can be significantly different from the theoretical estimates. Here, we describe an injection analysis to better characterize our survey’s sensitivity.

### 3.1. Injection of Single Pulses

We used the same data set (12 distinct and calibrated observations) that was used by Lazarus et al. (2015) and injected synthetic signals into those observations as previously described. A pulse was injected every  $\sim 10$  s, yielding 26 pulses per observation (of duration 268 s). In a single observation, all the injected pulses had the same parameters (i.e., pulse width, DM, and amplitude). Since the data quality can vary during an observation due to RFI, our method helps us characterize our sensitivity over the entire observation and provides a large statistical sample of pulses from which to draw conclusions. Even though the injected pulses within an observation had the same parameters, we repeated the process with a new set of parameters that allowed us to span a wide range of pulse characteristics (see Table 2) for our analysis. In order to vary the pulse width in the injection algorithm used by Lazarus et al. (2015), all pulses were



**Figure 2.** PALFA’s sensitivity to single pulses in the absence of scattering. Plotted is the minimum detectable peak flux density as a function of pulse width in the absence of pulse broadening due to scattering (left) and the ratio of the measured flux density limit to the predicted flux density limit (right). The dotted lines show the theoretical predictions as given by Equation (1), and the points show the actual detections where  $>90\%$  of the injected pulses with  $S/N > 7$  were recovered by the pipeline. The points have been connected by straight lines to guide the eye. The different colors correspond to different DMs in the range of  $\sim 42\text{--}5600\text{ pc cm}^{-3}$ . The sensitivity curves in the right-hand plot show that for pulse widths  $<5\text{ ms}$ , our survey is at most a factor of  $\sim 2$  less sensitive to single pulses than the theoretical predictions. For pulse widths  $>10\text{ ms}$ , as the DM decreases, the relative degradation in sensitivity can increase up to a factor of  $\sim 4.5$ .

injected using the same duty cycle of  $\sim 1.5\%$ , but with different pulse periods. For the first set of injection trials, the injected pulses were not subject to scatter-broadening. In the second set of injections, we fixed the DM and pulse width and varied scattering times.

### 3.2. Results of Sensitivity Analysis

The data with injected pulses were processed by the single-pulse pipeline described in Section 2. Every pulse in a single observation was injected with an amplitude corresponding to an initial best guess for the limiting flux density. The output of the pipeline was classified as either a detection or a non-detection. Since all injected pulses in a single observation were given the same amplitude, the pipeline output was classified as a detection if at least 24 of the 26 injected pulses in a single observation were successfully detected with  $S/N > 7$ , giving us  $>90\%$  confidence of detecting a single pulse above  $S/N$  of 7. In this case, we reduced the amplitude by 20% for the next injection trial. In case of a non-detection, the flux of the single pulses was increased by 20% for the next injection trial. The injected flux was varied in this way until the difference between the fluxes of outputs classified as a “detection” and a “non-detection” was less than 10%. The injected flux at this point was assigned to be the sensitivity limit for the corresponding set of injection parameters, and the observation used the median of the sensitivity limits from all 12 observations, declared to be the survey’s minimum detectable peak flux density for the corresponding set of injection parameters (i.e., DM, pulse width, and scattering time).

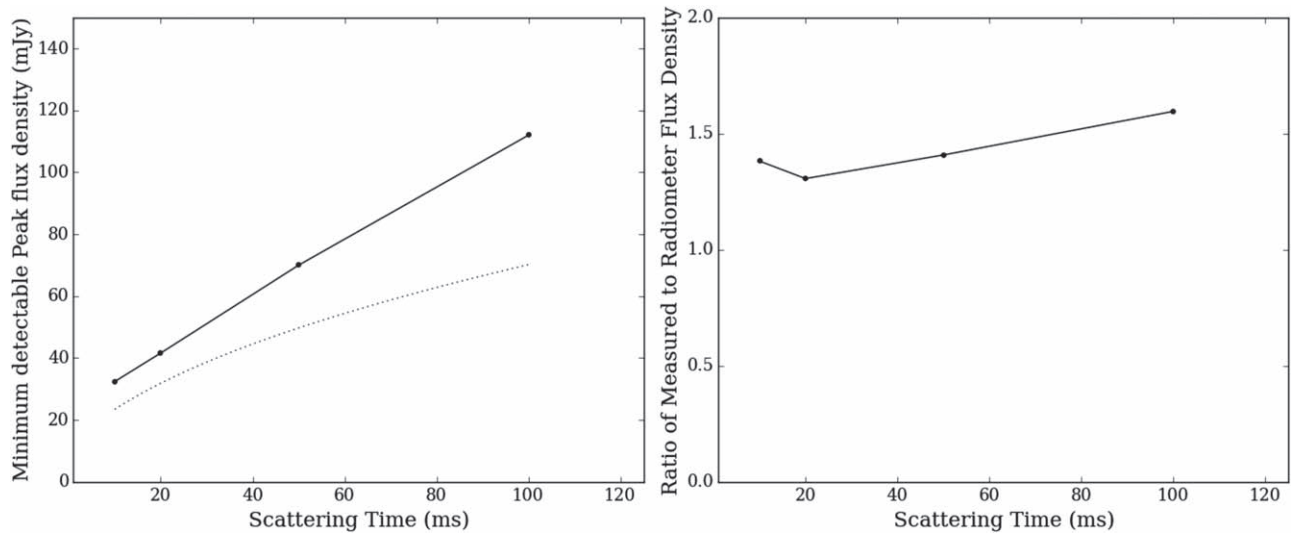
We show the results of the sensitivity analysis in the absence of scattering in Figure 2. As expected from the theoretical predictions, the minimum detectable flux density increases with DM for all pulse widths. For all DMs, it decreases as the pulse width increases. The comparison between the measured and the theoretical sensitivities of the survey is shown in the right plot of Figure 2. For low pulse widths ( $<5\text{ ms}$ ), the survey suffers a degradation in sensitivity by a factor of  $\sim 1.5$  at low DMs to  $\sim 2$

at high DMs, compared to the theoretical estimates. For low pulse widths and high DMs, this loss in sensitivity is primarily due to intra-channel smearing. We also find that for large pulse widths ( $>5\text{ ms}$ ), as the DM decreases, the degradation in sensitivity increases to a factor of  $\sim 4.5$  from the theoretical predictions. We understand that this can be attributed to zero-DM filtering (Eatough et al. 2009) that we perform to mitigate broadband terrestrial RFI. While this technique is excellent at mitigating terrestrial RFI, it also removes power from astrophysical signals at low DMs.

Next we introduced scattering to the injected pulses assuming  $DM = 1005.7\text{ pc cm}^{-3}$  and a pulse width of 5 ms in the same data set. For PALFA pointings, scattering timescales at high DMs can range from a few microseconds (if pointing at high Galactic latitudes toward the outer Galaxy) to a few seconds (for low Galactic latitudes toward the inner Galaxy). Since PALFA does not search for pulse widths  $>100\text{ ms}$ , the scattering timescales for this analysis were less than 100 ms. The injection parameters are shown in Table 2. Again, 26 pulses were injected for a single trial, with a detection declared if at least 24 pulses with  $S/N > 7$  were recovered by our single-pulse pipeline. The results of this analysis are shown in Figure 3. The sensitivity of our survey to single pulses for these parameters is a factor of  $\sim 1.5$  lower than that predicted by Equation (1). This is roughly the same amount of degradation that we find for single pulses (pulse widths 5 ms and  $DM \sim 1000\text{ pc cm}^{-3}$ ) that are not subject to scattering (see Figure 2, right). This indicates that Equation (1) adequately models the effects of scattering.

## 4. New Discoveries and Candidates

The new single-pulse pipeline has been fully incorporated into our main data analysis pipeline since 2015 July, during which we have processed  $\sim 60,500$  beams as of 2018 February 10. With seven beams per PALFA survey pointing and with each being 268 s long in the inner Galaxy and 180 s long in the outer Galaxy, we have just under 24 days of total observing



**Figure 3.** PALFA’s sensitivity to single pulses in the presence of scattering for  $DM = 1005.7 \text{ pc cm}^{-3}$ . We plot the minimum detectable flux density as a function of scattering times when pulse broadening is dominated by scattering (left) and its ratio to the theoretical prediction (right) based on Equation (1). The injections were done for a single DM and a single intrinsic pulse width. The dotted line is the theoretical prediction given by Equation (1), and the solid line is the actual “detection” limit, for which  $>90\%$  of the injected pulses with  $S/N > 7$  were recovered by the pipeline. The curve shows that for this set of parameters, the survey’s sensitivity is degraded by less than a factor of two from the theoretical prediction.

time. From the number of beams processed, this pipeline has reported a total of  $\sim 900,000$  single-pulse candidates (grouped single pulses). Out of these,  $\sim 55,000$  single-pulse candidates have been classified by members of the PALFA collaboration with our web viewer (Section 2.6) using a variety of filters and ratings (Section 2.4). Of the classified candidates,  $\sim 46,000$  have been classified as being RFI or noise,  $\sim 3800$  have been classified as potential astrophysical candidates, and  $\sim 4900$  have been classified as known astrophysical sources. The single-pulse pipeline has uniquely discovered three pulsars (two RRATs and one pulsar). Additionally, it has independently discovered six pulsars which were also detected using our standard periodicity analysis. It has also identified three candidate RRATs and one candidate FRB (see Section 6). The details of the new discoveries are presented in Table 3, and their dedispersed frequency versus time plots are shown in Figure 4. The  $w_{50}$  (full width at half maximum) and  $w_{90}$  (full width at a tenth of the maximum) pulse widths for each discovery candidate were estimated by fitting a Gaussian to their pulse profiles. In order to estimate the peak flux densities reported in Table 3, we used the radiometer equation (Equation (1)), for which we used  $T_{\text{sys}} + T_{\text{sky}} = 30 \text{ K}$ , telescope gain  $G = 8.2 \text{ K Jy}^{-1}$  (Spitler et al. 2014),  $\beta = 0.9$ ,  $n_p = 2$ , and  $\Delta f = 322 \text{ MHz}$ . The  $S/N$  and  $w_{90}$  (used as  $W_b$ , the broadened pulse width) were taken from Table 3. For each source, we estimated the degradation factor by choosing the right-hand curve in Figure 2 corresponding to the nearest DM value, and the factor (ratio of measured to radiometer flux density limit) corresponding to its pulse width. We then applied the degradation factor to the peak flux density estimated by the radiometer equation.

All the discoveries in the upper section of Table 3 have been confirmed via re-observations and are now being monitored by either the Lovell Telescope at Jodrell Bank Observatory or with Arecibo Observatory as a part of our timing campaign. Their detailed timing properties will be reported in a future publication.

## 5. Population Synthesis of RRATs in the PALFA Survey

To predict the number of RRATs detected by the survey, we follow the approach for the RRAT population model developed by D. Agarwal et al. (2018, in preparation), who have recently adapted the pulsar population software PSRPOPpy2<sup>25</sup> (Bates et al. 2014) to model the Galactic population of RRATs. In their optimal model for the underlying RRAT population, when passed through model surveys, the resulting model-detected population closely resembles the observed RRAT population.

This model is based on RRATs detected by four surveys with the Parkes telescope in Australia: the Parkes multibeam survey (Manchester et al. 2001; McLaughlin et al. 2006; Keane et al. 2011), the high time resolution intermediate survey (Keith et al. 2010; Burke-Spolaor et al. 2011), and two higher latitude surveys (Edwards et al. 2001; Jacoby et al. 2009; Burke-Spolaor & Bailes 2010). We follow a method similar to the method used by Lorimer et al. (2006) for constructing a “snapshot” (i.e., no time evolution) of the underlying RRAT population. We begin with uniform underlying distributions for the period, luminosity,  $L$ , Galactocentric radius,  $R$ , Galactic scale height,  $Z$ , and burst rate. A total of 1100 RRATs is drawn with these distributions and run through the surveys mentioned previously. This number is much higher than the actual number detected through the surveys to minimize statistical fluctuations. The properties of the model-detected population are then compared with the RRATs detected from these surveys by calculating the reduced  $\chi^2$  of the distributions in  $R$ ,  $L$ ,  $Z$ , and burst rate. As described in Lorimer et al. (2006), correction factors are applied to the underlying population to refine the models, and the process is repeated until the reduced  $\chi^2$  between the observed and detected model population is  $\sim 1$ . Full details of this analysis are given in D. Agarwal et al. (2018, in preparation).

Using the optimal model parameters from this procedure, we generate a population such that it detects 54 RRATs (the actual number detected) in the four surveys. We then run inner and outer Galaxy PALFA surveys to find the number of RRATs

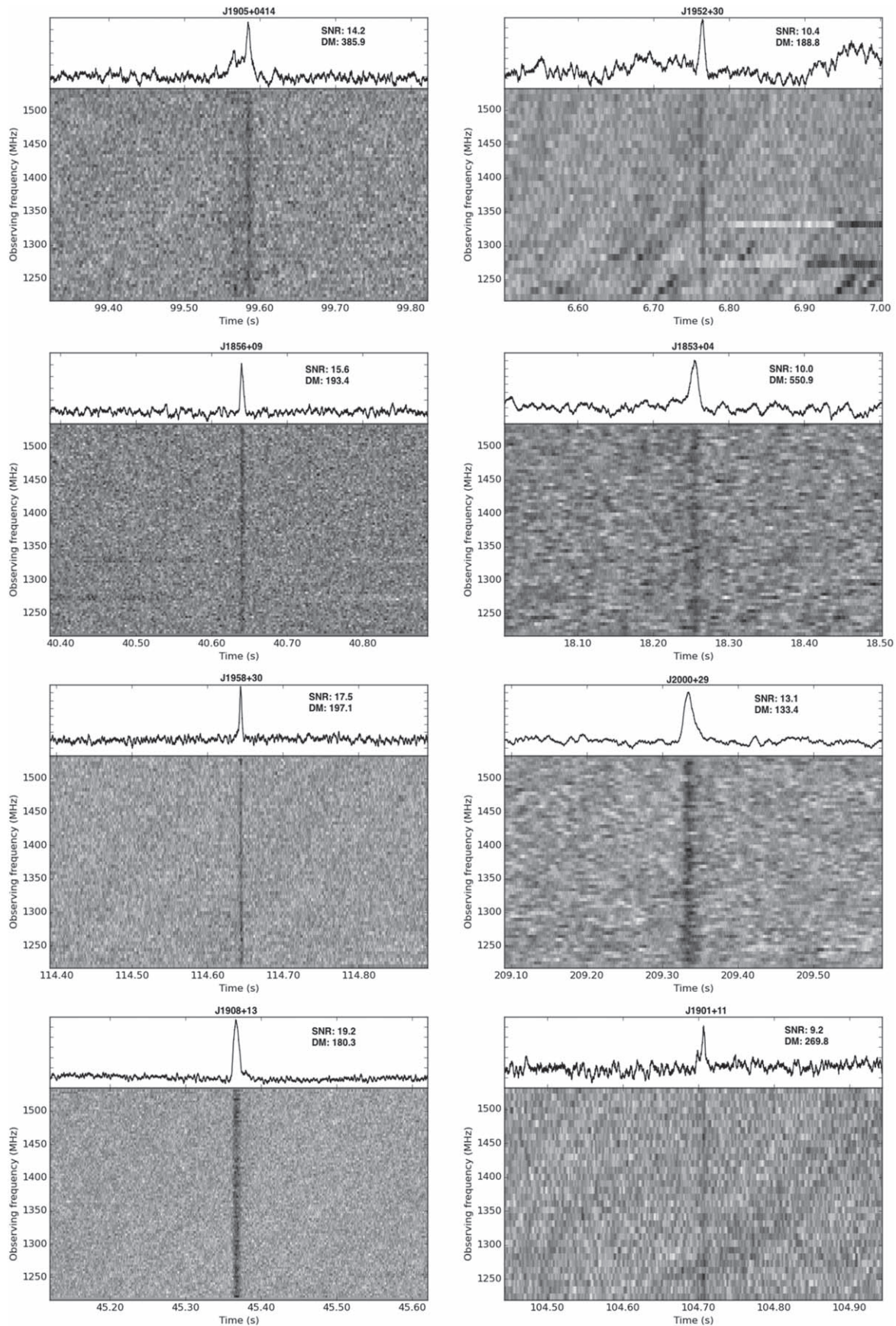
<sup>25</sup> <https://github.com/devanshkv/PsrPopPy2>

**Table 3**  
New Discoveries from the Single-pulse Pipeline

Name	Detection Method	Pulse Width (ms)		Period (ms)	DM (pc cm <sup>-3</sup> )	S/N	Degradation Factor	Flux Density (mJy)
		$w_{50}$	$w_{90}$					
PSR J1859+07	SP	4.5	8.1	...	$303.1 \pm 2.2$	9.2	1.5	20
PSR J1905+0414	SP	3.3	5.9	...	$383 \pm 1$	14.2	1.5	36
PSR J1952+30	SP	5.7	10.5	$1665.60 \pm 0.12$	$188.8 \pm 0.6$	10.4	2.5	33
PSR J1856+09	SP and Periodicity	4	7.3	$2170.71 \pm 0.11$	$193.4 \pm 0.6$	15.6	2	48
PSR J1853+04	SP and Periodicity	2	3.8	$1320.65 \pm 0.04$	$549.3 \pm 1.3$	10.0	1.5	33
PSR J1958+30	SP and Periodicity	4	7.3	$1098.53 \pm 0.02$	$199.3 \pm 0.4$	17.5	2	54
PSR J2000+29	SP and Periodicity	7.4	13.5	$3073.70 \pm 0.14$	$132.5 \pm 1.4$	13.1	3	159
PSR J1901+11	SP and Periodicity	2.2	4	$409.14 \pm 0.01$	$268.9 \pm 0.8$	9.2	1.5	29
PSR J1843+01	SP and Periodicity	3.5	6.4	$1267.02 \pm 0.04$	$247.8 \pm 2.4$	8.5	1.5	21
Candidate PSR J0625+12	SP	7.1	12.9	...	$101.9 \pm 6.1$	10.3	3	36
Candidate PSR J0623+15	SP	14.1	25.7	...	$92.5 \pm 1.6$	8.5	4.5	32
Candidate PSR J1908+13	SP	5.1	9.2	...	$180.3 \pm 1.1$	19.2	2	52
Candidate FRB 141103	SP	1.1	2	...	$400 \pm 3$	8.4	1.5	39

**Note.**

<sup>a</sup> The flux densities were calculated assuming that the pulses were detected in the center of the beams.



**Figure 4.** Dedispersed frequency vs. time plots for pulsars and RRATs discovered by the single pulse pipeline. The instrument bandpass has been subtracted.



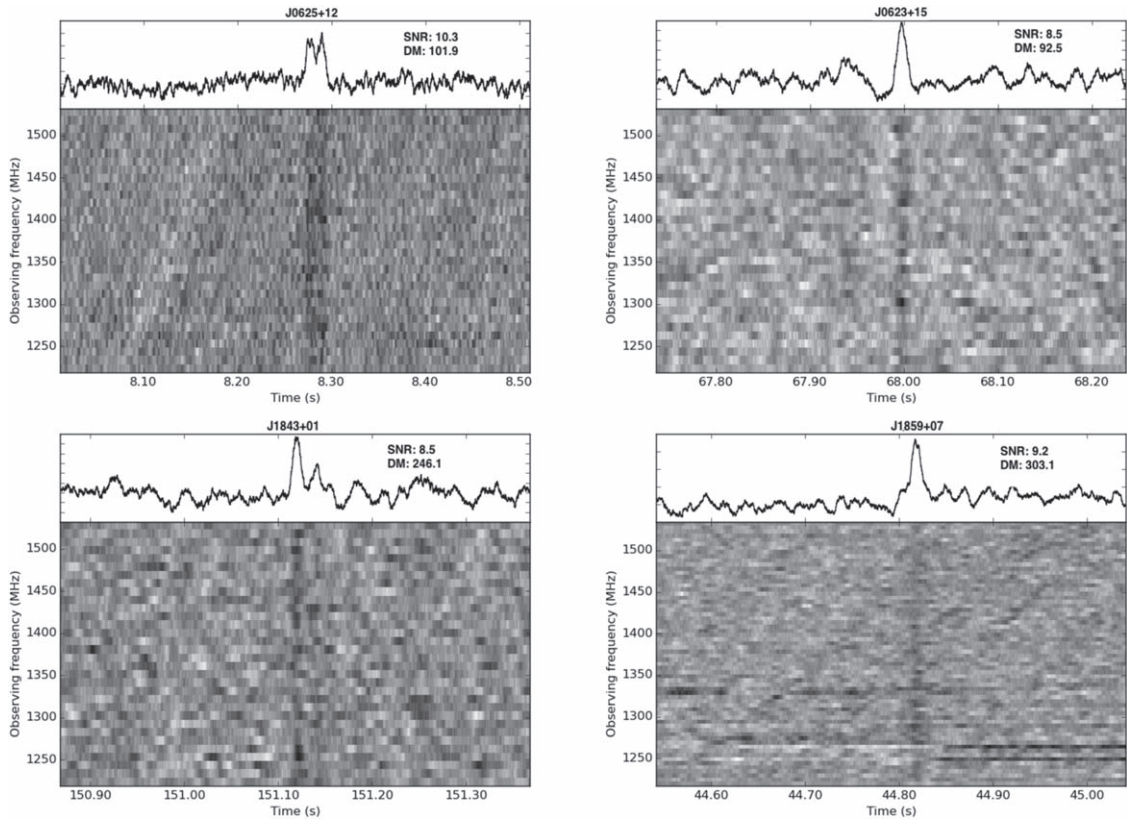


Figure 4. (Continued.)

detected. This process is repeated 1000 times to get a distribution of the number of RRATs detectable by PALFA. Figure 5 shows the distribution of the number of detected RRATs by the inner Galaxy survey. The distribution is fit with a Gaussian distribution with a mean  $\mu = 10.55 \pm 0.08$  and standard deviation  $\sigma = 3.30 \pm 0.08$ .

As shown in Figure 5, this simulation is in good agreement with the number of RRATs we find for the inner Galaxy survey. The same procedure was repeated for the outer Galaxy survey, and from this we predict zero detections. This appears to be in tension with the PALFA detections of two RRATs in the outer Galaxy. Although partially attributable to small number statistics, the discrepancy could be an indication that the population model is biased toward RRATs in the inner Galaxy. The four surveys used in constructing the model targeted the inner Galaxy. In the future, we will use discoveries from the PALFA survey to construct an improved RRAT population model.

## 6. Candidate FRB 141113

While manually classifying single-pulse candidates to use as a training set for our machine-learning classifier (Section 2.5), we identified a candidate fast radio burst. The burst (Figure 6) was detected at 2014 November 13 07:42:55.220 UTC (at 1537 MHz) with  $DM = 400.3 \text{ pc cm}^{-3}$ , width  $W \approx 2 \text{ ms}$ , and  $S/N = 8.4$  ( $S_{\text{pk}} = 39 \text{ mJy}$ ). The observed burst DM exceeds the Galactic maximum predicted along the line of sight ( $\ell = 191^\circ.9$ ,  $b = +0^\circ.36$ ) by both the NE2001 model ( $DM_{\text{NE,max}} = 188 \text{ pc cm}^{-3}$ ; Cordes & Lazio 2003) and the YMW16 model ( $DM_{\text{YMW16,max}} = 296 \text{ pc cm}^{-3}$ ; Yao et al. 2017); we therefore classify it as a candidate FRB and refer to

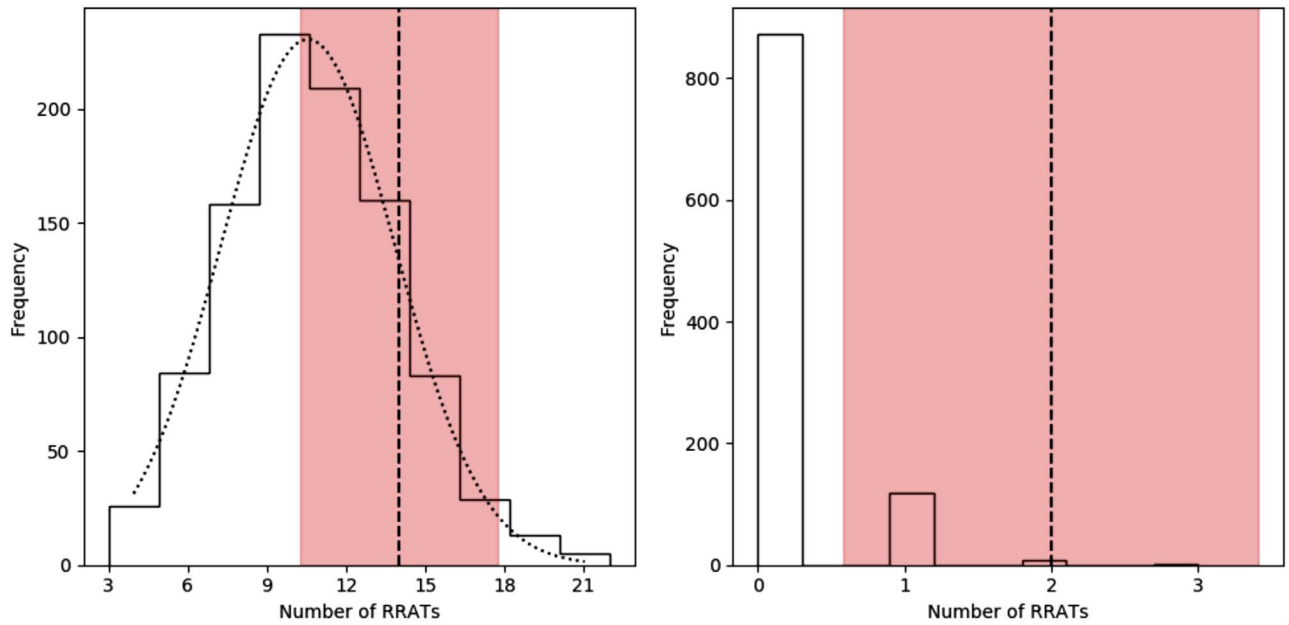
the burst as FRB 141113. To further investigate the reality of the event, we consider in detail both the significance of the burst detection and the robustness of the DM excess.

### 6.1. Candidate Significance

The false-alarm probability of a single-pulse detection at  $S/N = 8.4$  due purely to Gaussian noise is vanishingly small. In the presence of RFI, however, statistical probabilities can be difficult to quantify reliably. To assess the significance of our detection of FRB 141113, we manually classified *all* candidates in the database with  $S/N \geq 7$ ,  $DM = 300\text{--}3000 \text{ pc cm}^{-3}$  ( $DM = 2596 \text{ pc cm}^{-3}$  is the highest DM of all FRBs known to date; Bhandari et al. 2018) and  $W \leq 10 \text{ ms}$  (only 3 out of 30 FRBs have  $W > 10 \text{ ms}$ ).<sup>26</sup> The manual classification was done by visually inspecting the single-pulse candidate (“spd”) plot of each of the candidates that met our selection criteria and determining whether the candidate appeared astrophysical based on its frequency structure (broadband and well described by a  $\nu^{-2}$  law characteristic of cold plasma dispersion).

A distribution of the  $\approx 5000$  manually classified candidates as a function of  $S/N$  is shown in Figure 7. The top panel shows the distribution of all the  $\approx 270$  candidates classified as likely astrophysical (some of which have already been confirmed as astrophysical via re-observations) by members of the collaboration. The middle panel shows the distribution of the  $\approx 4500$  candidates classified as RFI or noise, and the bottom panel shows the distribution of  $\approx 270$  pulses from known astrophysical sources.

<sup>26</sup> <http://frbcat.org/>



**Figure 5.** Distribution of the number of detected RRATs with the inner (left) and outer (right) Galaxy PALFA survey for 1000 iterations. The dashed vertical line represents the number of RRATs detected in each survey. The red shaded region represents Poissonian  $\sqrt{N}$  uncertainties in the number of detected RRATs. The dotted line in the left plot shows the Gaussian fit for the distribution for the inner Galaxy survey (see the text).

Bright potential astrophysical candidates look qualitatively very different from RFI (or noise) candidates and so are reliably classified. However, weaker potentially astrophysical signals are harder to distinguish from noise. Such candidates are conservatively classified as noise. The distribution of candidates from known sources is relatively flat compared to the other distributions because most of the known sources have multiple single pulse candidates that span a wide range of S/N.

Importantly, *all* candidates with S/N > 8 classified as potential astrophysical sources have indeed been confirmed as pulsars or RRATs via re-observations, except FRB 141113. We henceforth assume the source to be astrophysical.

## 6.2. Galactic DM Contribution

We next consider whether candidate FRB 141113 is extragalactic (i.e., a genuine FRB), or whether its excess DM could be caused by an intervening Galactic source not accounted for in the electron density models.

### 6.2.1. Multiwavelength View of FRB Region

We search for HII regions along the line of sight to FRB 141113 on angular scales from  $\lesssim 1''$  to  $\approx 1^\circ$  using both archival multiwavelength data and a new VLA observation. Figure 8 shows the FRB field on two angular scales (2.5' and 30') in the mid-infrared (useful to search for HII regions), H $\alpha$  (a tracer of ionized gas), and 1.4 GHz radio (for free-free emission) bands. The seven  $\theta_{\text{FWHM}} = 3.5'$  PALFA beams are shown in each panel, with the detection beam indicated by a solid circle.

The mid-infrared panels of Figure 8 show 12  $\mu\text{m}$  (green) and 22  $\mu\text{m}$  (red) data from the *WISE* survey (Wright et al. 2010). In the 2.5' image, there are several structures with nebular morphology, notably a well-known complex of HII regions (S254-258; Chavarría et al. 2008) about 45' south of the FRB detection beam and another about 20' to the east. Most (if not all) of these regions lie within the Gemini OB1 molecular

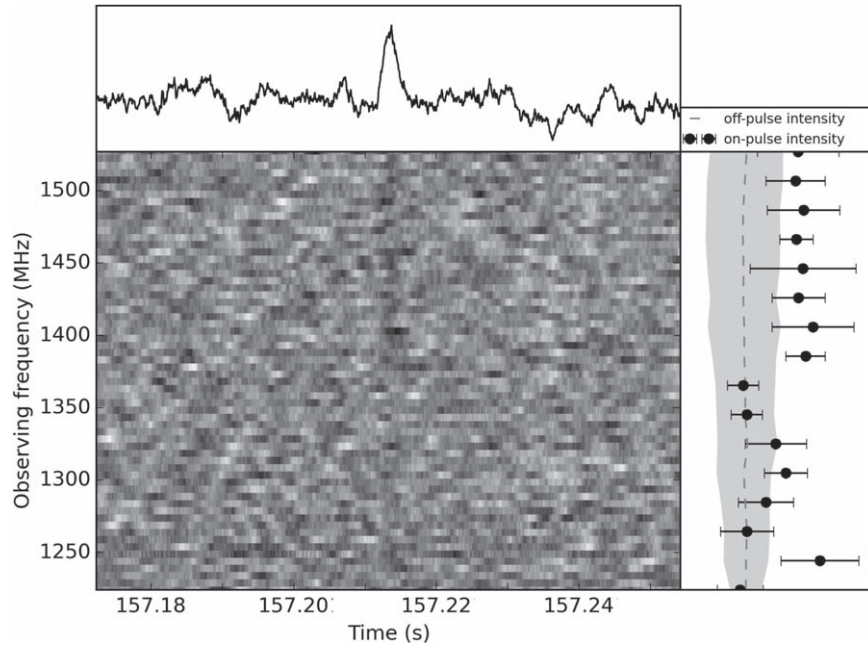
cloud complex at a distance of  $d \approx 2$  kpc from the Sun (Carpenter et al. 1995). In the 30' image, there is a bright imaging artifact  $\approx 5'$  south, but no obvious HII regions near the detection beam.

The H $\alpha$  panels of Figure 8 show data from the Virginia Tech Spectral-line Survey (VTSS, Draper et al. 1993) in the 2.5' field and IPHAS (Drew et al. 2005) in the 30' field. The VTSS image clearly shows the S254-258 HII regions. It also shows a large ( $\theta \approx 0.8$  diameter) faint ( $I_{\text{H}\alpha} \approx 10\text{--}20 R^{27}$ ) structure that just barely overlaps the detection beam. The IPHAS 30' image shows that while the brightest regions are to the northeast, there is still an elevated H $\alpha$  flux coincident with the detection beam.

The 1.4 GHz radio panels of Figure 8 show data from the Parkes CHIPASS map (Calabretta et al. 2014) in the 2.5' field and VLA NVSS data (Condon et al. 1998) in the 30' field. The CHIPASS map shows an increase in the full-beam ( $\theta_{\text{HPBW}} = 14'$ ) brightness temperature of  $\Delta T_b \approx 100\text{--}200$  mK ( $S \approx 0.2\text{--}0.5$  Jy beam $^{-1}$  with  $G = 0.44$  K Jy $^{-1}$ ) at roughly the same position as the H $\alpha$  peak. From the NVSS map, however, we see that a Parkes beam at this location would contain three point sources with total flux density of  $S_{\text{sum}} \approx 0.2$  Jy accounting for the rise in flux in the CHIPASS map. There are no sources seen within the detection beam in the NVSS map.

In addition to archival radio data, we also conducted observations with the Karl G. Jansky Very Large Array (VLA) to produce a sensitive radio map on arcsecond scales. Observations were conducted on 2018 January 22 (MJD 58140) at 1–2 GHz with the array in B-configuration and resulted in about 12 minutes of time on source. The absolute flux density calibrator 3C138 and the phase calibrator J0534+1927 were used. The data were calibrated and flagged using the VLA calibration pipeline. Additional RFI flagging and self-calibration were done after the pipeline calibration to produce a final primary-beam corrected image (Figure 9) with rms noise of  $\sigma \approx 30$   $\mu\text{Jy beam}^{-1}$  in the center of beam, which is consistent with expectations.

<sup>27</sup>  $1 R = 10^6/4\pi$  photons cm $^{-2}$  s $^{-1}$  sr $^{-1}$ .



**Figure 6.** Dedispersed frequency vs. time plot for the candidate FRB 141113. The pulse was detected at 2014 November 13 07:42:55.220 UTC (at 1537 MHz) with  $S/N = 8.4$ , pulse width  $\sim 2$  ms, and  $DM = 400 \text{ pc cm}^{-3}$  (well above the Galactic contribution). For clarity, we used a frequency resolution of 64 sub-bands. The instrumental bandpass has been subtracted. On the right are mean on-pulse (scatter points) and off-pulse (dashed line) relative intensities binned over 16 sub-bands. The on-pulse area was taken to be the  $W_{90}$  (from Table 3) region around the peak of the pulse. The remainder was considered as an off-pulse region. The gray band shows the  $1\sigma$  range around the mean of the off-pulse intensity. The error bars on the scatter points indicate  $1\sigma$  spread around the mean of the on-pulse intensity.

### 6.2.2. DM Contribution from a Galactic Nebula?

The excess DM FRB 141113,  $\Delta DM = DM - DM_{\text{mod}}$ , is  $\Delta DM_{\text{NE}} = 212 \text{ pc cm}^{-3}$  for NE2001 and  $\Delta DM_{\text{YMW16}} = 104 \text{ pc cm}^{-3}$  for YMW16. We explore whether there could exist an unmodeled Galactic ionized region contributing to this excess along the line of sight to FRB 141113, and set limits in various wavebands on any relevant emission.

A hypothetical homogeneous spherical nebula along the FRB sight-line with  $\Delta DM = 212 \text{ pc cm}^{-3} = n_e L_{\text{pc}}$  ( $L_{\text{pc}}$  is the nebula size in parsecs) would have an emission measure of at least  $EM = \Delta DM^2 / L_{\text{pc}} = 45000 \text{ pc cm}^{-6} L_{\text{pc}}^{-1}$ . For an electron temperature of 8000 K, the nebula has a free-free optical depth of

$$\tau_{\text{ff}} = \frac{0.01}{L_{\text{pc}}} \left( \frac{T_e}{8000 \text{ K}} \right)^{-1.35} \left( \frac{\nu}{1.4 \text{ GHz}} \right)^{-2.1}. \quad (2)$$

Since an optically thick nebula is rendered implausible by the absence of a detection of any ultra-compact H II region in the *WISE* H II region survey (Anderson et al. 2014), we require that the nebula be optically thin. This requirement sets a lower limit of  $L_{\text{min}} = 0.01 \text{ pc}$  on the size of the nebula. Introducing a filling factor in the expressions for  $\Delta DM$  and EM only makes the limits below more constraining (Kulkarni et al. 2014).

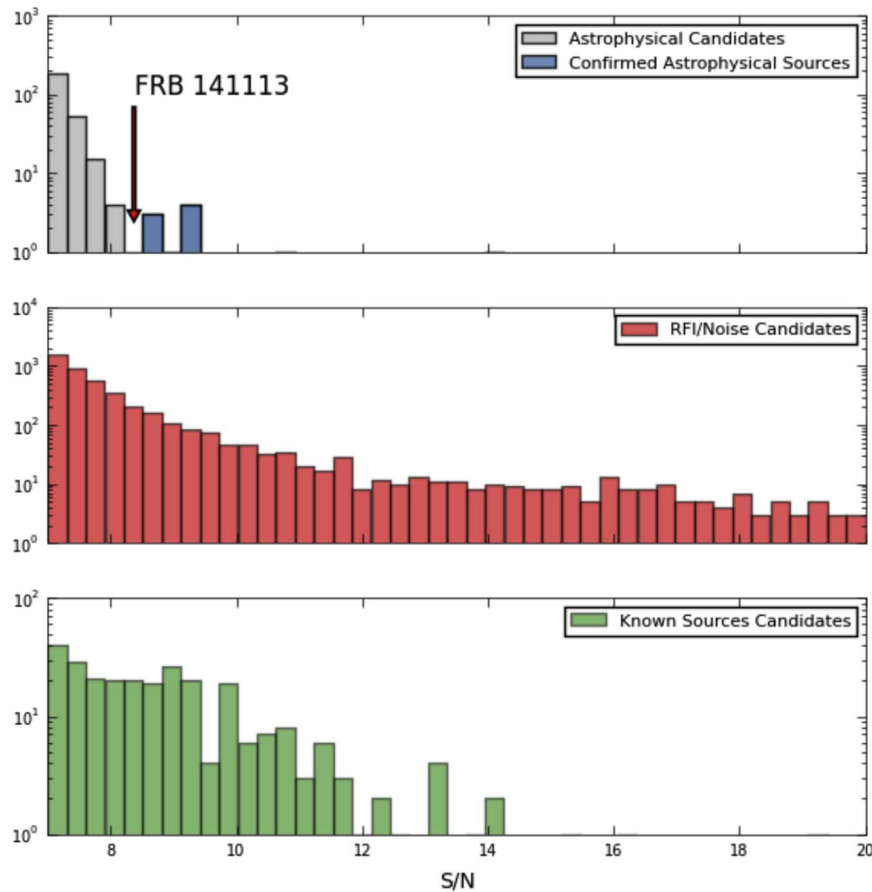
Using the IPHAS point source catalog (Drew et al. 2005), we search for  $H\alpha$  emission from a compact nebula. Following the method described in Kulkarni et al. (2015) and Scholz et al. (2016), we estimate that the  $H\alpha$  flux for a compact nebula at 20 kpc in standard IPHAS magnitude units ( $ha$ ) would be  $ha < 17$ . This assumes  $L_{\text{pc}} = 0.01 \text{ pc}$ , imposed by the optically thin condition (Equation (2)). From the IPHAS point source catalog, there are 1135 cataloged sources in  $5'$  radius regions around the nominal FRB position, out of which 159 objects have  $ha < 17$ . None is classified as an  $H\alpha$  emitter

(Barentsen et al. 2014). Another method of classifying  $H\alpha$  emitters is with a color-color diagram (Kulkarni et al. 2015). For the FRB region, this is shown in Figure 10. Any sources lying above the cluster of points would be  $H\alpha$  emitter candidates. However, we see none having  $ha < 17$ . Therefore, IPHAS strongly constrains the presence of an unresolved Galactic nebula in the FRB region. Assuming a larger nebula or closer distance would strengthen this conclusion.

Next, we consider the free-free emission from a nebula that contributes the excess DM seen toward FRB 141113. Following Scholz et al. (2016), we calculate the 1.4 GHz flux density as a function of nebula size (Figure 11). In order to cover a wide range of angular sizes, we use data from our newly observed VLA B-configuration observations ( $\theta_B = 4''$ ), archival VLA NVSS data ( $\theta_{\text{NVSS}} = 45''$ ), and single dish Parkes data from CHIPASS ( $\theta_P = 14'.4$ ).

At the largest angular scales, we set a limit of  $S_{\text{max}} = 0.3 \text{ Jy}$  in the Parkes beam (HPBW =  $14'.4$ ), as discussed in Section 6.2.1. At smaller angular scales, we can use VLA observations. In the NVSS map ( $\theta_{\text{HPBW}} = 45''$ ,  $\sigma = 0.4 \text{ mJy beam}^{-1}$ ), there are no sources detected above  $5\sigma$  in the PALFA burst detection beam ( $\theta_{\text{HPBW}} = 3'.5$ ). The nearest detected source is  $5'$  from the center of the burst detection beam and falls within another PALFA beam (Figure 8). We set a  $5\sigma$  upper limit of  $S_{\text{max}} = 2 \text{ mJy beam}^{-1}$  from the NVSS map.

In the VLA B-configuration map ( $\theta_{\text{HPBW}} = 4''$ ,  $\sigma = 30 \mu\text{Jy beam}^{-1}$ ), there are no sources detected above  $5\sigma$  in the PALFA burst detection beam. Searching out to  $\Delta\theta = 5'$  (a distance that would roughly include the sidelobes of one PALFA beam), we find nine sources (Figure 9). Five are located closer to a PALFA beam in which there was no detection, so we exclude these from consideration. None of the four remaining (sources 1, 2, 7, 8) is reported as having  $H\alpha$  emission in the IPHAS point source catalog. Hence, these are



**Figure 7.** S/N distribution of candidates with  $S/N \geq 7$ , DM between  $300 \text{ pc cm}^{-3}$  and  $3000 \text{ pc cm}^{-3}$  and pulse width  $\leq 10 \text{ ms}$  as manually classified by members of PALFA collaboration. Top: Potential astrophysical candidates (totaling  $\approx 270$ ) showing that FRB 141113 uniquely stands out from the population. Middle: Candidates classified as RFI or noise (totaling  $\approx 4450$ ). Bottom: Single pulses from known sources (totaling  $\approx 270$ ). Note that there are multiple events for most known sources and that the vertical scale is not the same in each panel.

unlikely to be HII regions. We set a  $5\sigma$  upper limit of  $S_{\text{max}} = 150 \mu\text{Jy beam}^{-1}$  from the VLA B-configuration map.

### 6.2.3. Galactic or Extragalactic?

Figure 11 shows the predicted free-free emission from a nebula at 10 kpc accounting for the DM excess  $\Delta\text{DM}$  seen toward FRB 141113 for both the NE2001 and YMW16 electron density models. Using limits from the free-free radio emission,  $\text{H}\alpha$  emission, and the optically thin plasma requirement, we exclude nebulae with angular sizes of up to several degrees out to 10 kpc, assuming the NE2001 excess. The smaller DM excess predicted by the YMW16 model allows for the possibility that an extended ( $\theta \gtrsim 15'$ ) and distant ( $d \geq 8 \text{ kpc}$ ) nebula contributes the observed DM excess. An extended ( $\theta \approx 0.8^\circ$ ) source is seen in the  $\text{H}\alpha$  image (Figure 8), but it is almost certainly associated with the Gemini OB1 molecular cloud complex at  $d \approx 2 \text{ kpc}$  and would be ruled out by the free-free limits. Overall, we conclude that FRB 141113 is very likely extragalactic.

### 6.3. Host Galaxy and IGM Contribution

Assuming now that FRB 141113 is genuine and extragalactic, we calculate the host and IGM contributions to the observed DM as  $\text{DM}_{\text{IGM}} + \text{DM}_{\text{host}} = \text{DM} - \text{DM}_{\text{NE,max}} - \text{DM}_{\text{halo}} \approx 182 \text{ pc cm}^{-3}$  with  $\text{DM}_{\text{halo}} \approx 30 \text{ pc cm}^{-3}$  and  $\text{DM}_{\text{NE,max}} = 188 \text{ pc cm}^{-3}$ . Using the  $\text{DM}_{\text{IGM}}$ -redshift scaling relation

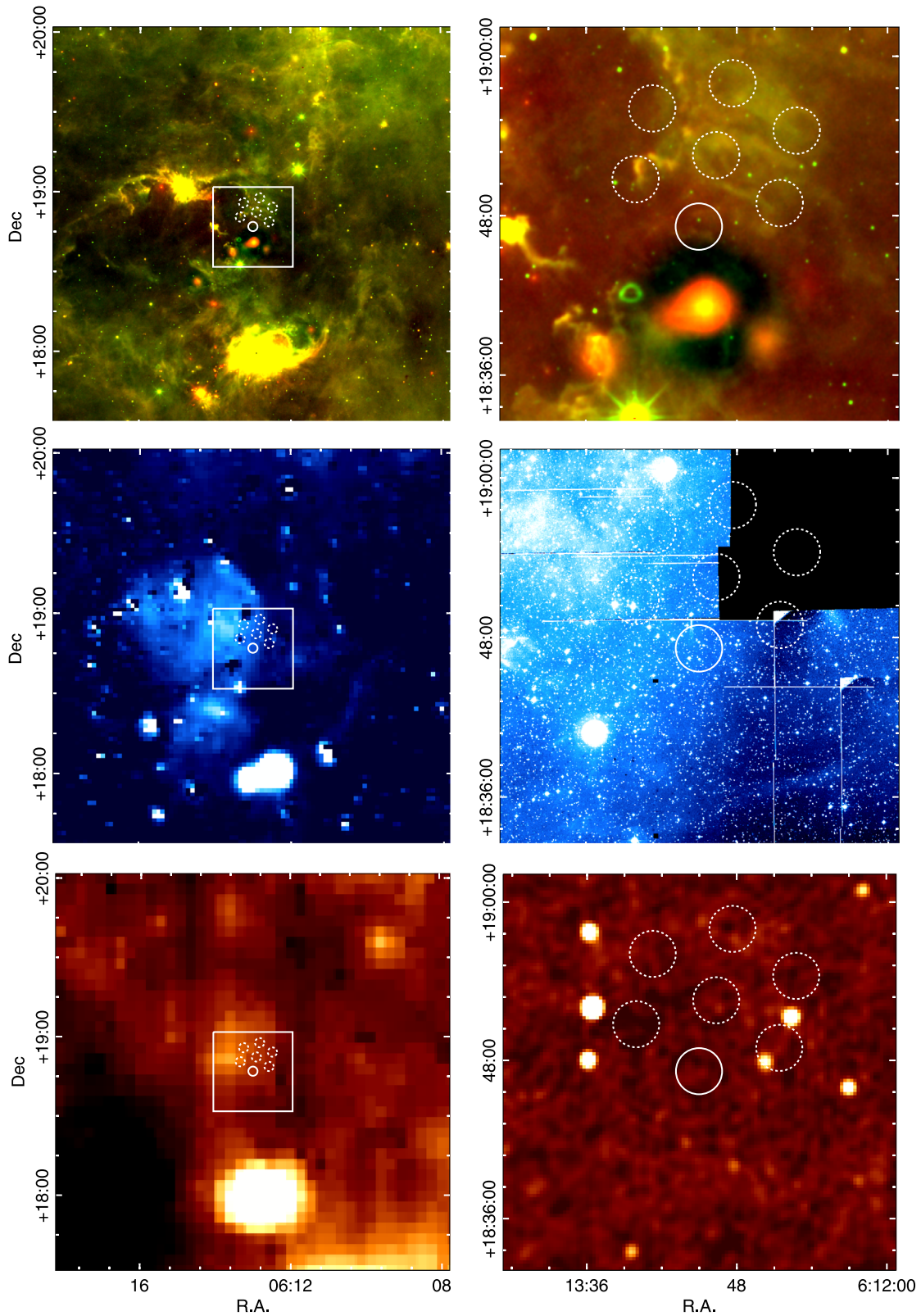
$\text{DM} \approx 1200z \text{ pc cm}^{-3}$  for  $z \leq 2$  (Ioka 2003; Inoue 2004), we estimate a redshift of  $z < 0.15$ , which corresponds to a distance of approximately 0.6 Gpc. This, and the low flux of 39 mJy (Table 3), suggest the FRB 141113 could be one of the closest FRBs with one of the lowest luminosities yet detected. However, detection in a sidelobe, which would imply a much larger source flux, cannot presently be excluded. If the source repeats, an interferometric position determination will be possible, and the true source flux could be established. Multiwavelength follow-up would be warranted, given its relatively nearby location compared with other FRBs. Monitoring observations are ongoing at the Arecibo Observatory.

## 7. Implications for the FRB Population

We have found that FRB 141113 is likely to be a genuine extragalactic cosmic event. An additional check on its authenticity is to verify whether its detection in PALFA is consistent with reported event rates and constraints on the flux density distribution of the FRB population.

### 7.1. FRB Detection Rate

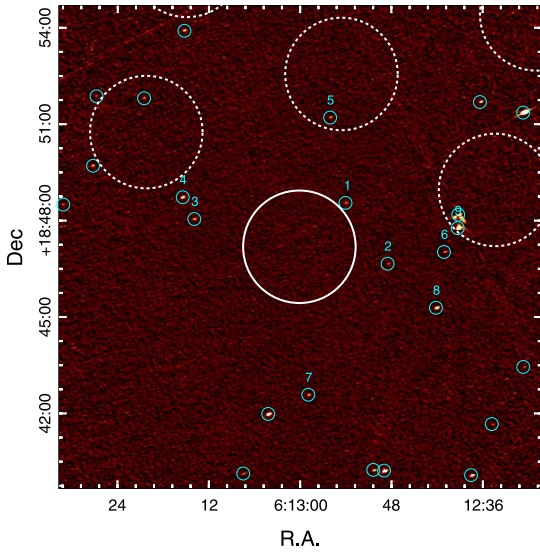
The sensitivity of the PALFA survey allows for the detection of bursts in the FWHM region of the beam (hereafter, main beam) and in the near sidelobes, thus requiring characterization of both to determine the FRB rate. For the main beam, the field of view (FOV) is  $\Omega = 0.022 \text{ sq. deg.}$ , and the mean system flux



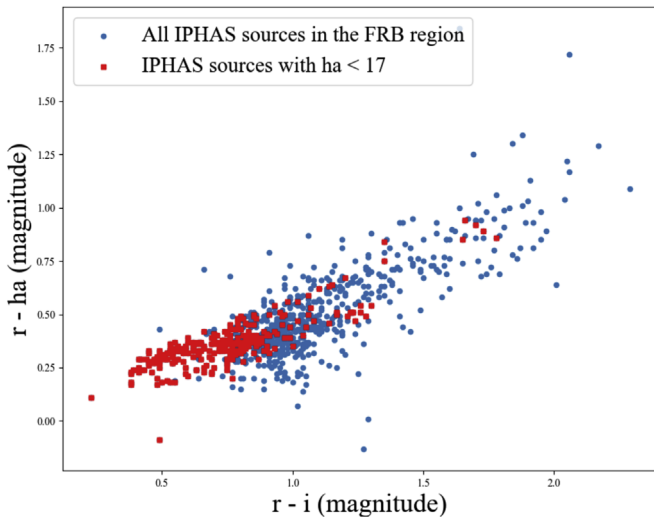
**Figure 8.** FRB 141113 field in infrared,  $H\alpha$ , and 1.4 GHz radio bands. The seven PALFA beams with  $HPBW = 3/5$  are shown (detection beam with solid line). The left column shows a  $2.5$  square patch of sky centered on the detection beam position, and the right column shows the  $30'$  region indicated by the white square in the left column. The top panels show *WISE*  $12 \mu\text{m}$  (green) and  $22 \mu\text{m}$  (red). The center panels show  $H\alpha$  data from VTSS (left) and IPHAS (right). The bottom panels show 1.4 GHz radio maps from CHIPASS (left) and NVSS (right).

$S_{\text{sys}} = 5 \text{ Jy}$ , and for the full FOV of  $0.105 \text{ sq. deg.}$ ,  $S_{\text{sys}} = 27 \text{ Jy}$ . The full FOV includes the main beam and regions of the near sidelobes with gain greater than the Parkes 1.4-GHz

average gain of  $0.4 \text{ K Jy}^{-1}$  (Spitler et al. 2014). Based on the previously mentioned system fluxes, S/N detection threshold of  $(S/N)_b = 8$ ,  $n_p = 2$ , and  $\Delta f = 322 \text{ MHz}$ , we estimate the



**Figure 9.**  $15' \times 15'$  VLA map of the FRB 141113 detection region at 1–2 GHz. The solid white circle shows the PALFA burst detection beam ( $\theta_{\text{HPBW}} = 3'.5$ ), and the dashed circles show the other beams. The cyan circles show sources detected above a  $5\sigma$  threshold of  $S_{\text{det}} = 150 \mu\text{Jy}$ . Sources within  $5'$  of the center of the detection beam are numbered in order of increasing angular separation from the detection beam.



**Figure 10.** Color–color diagram for the 1135 IPHAS sources in the FRB region. The sources shown as red squares ( $ha < 17$ ) are classified as either stars or galaxies. Moreover, there is no source having  $ha < 17$  lying above cluster of points, consistent with none being an  $H\alpha$  emitter.

minimum detectable flux densities for the main and full beams to be 44 mJy and 239 mJy, respectively. The calculation is performed using Equation (1) for an intrinsic pulse width of 3 ms, assuming no scatter-broadening, and accounts for the degradation in sensitivity by a factor of 1.5, as discussed in Section 3. Additionally, we adopt  $(S/N)_b = 8$  instead of 7, which was employed in the sensitivity analysis in Section 3, because of the ambiguity in determining whether a candidate with  $(S/N)_b < 8$  is RFI or astrophysical (see Figure 7).

We adopt  $T_{\text{obs}} = 24.1$  days as an estimate of the total observation time for PALFA pointings processed by the modified analysis pipeline. The estimate is obtained after subtracting time corresponding to the mean masking fraction due to RFI of 10%, assuming that all masking was done in the time domain. Additionally, pointings with masking fraction greater than 20% were not processed by the pipeline and hence were not included in the estimate. Although scattering in the inner Galaxy can hinder FRB detection, more than 97% of the included pointings have predicted maximum scattering time-scales of  $< 2$  ms along their line of sight, thus ensuring minimal effect on the results of the following analyses.

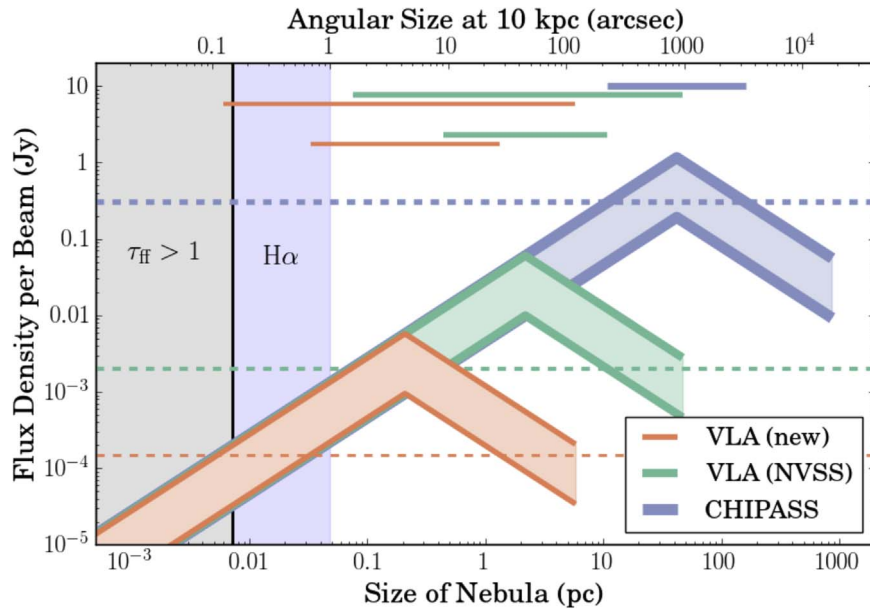
Based on the detection of one likely event (i.e., FRB 141113) in observations of 0.022 sq. deg. of sky for a duration of 24 days, we estimate the FRB detection rate for the main beam of the PALFA survey to be  $7.8^{+35.6}_{-7.6} \times 10^4$  FRBs  $\text{sky}^{-1} \text{day}^{-1}$  above a threshold of 44 mJy, with the 95% confidence interval evaluated assuming Poisson statistics. Accounting for the possibility of the burst being detected in the near sidelobes as for the repeating FRB 121102 (Spitler et al. 2014; Chatterjee et al. 2017), we estimate  $1.6^{+7.5}_{-1.6} \times 10^4$  FRBs  $\text{sky}^{-1} \text{day}^{-1}$  above a threshold of 239 mJy. The above estimate assumes uniform sensitivity to bursts with diverse spectral behavior, such as those detected from the repeating FRB 121102 (Scholz et al. 2016).

We have not updated the rate estimate reported by Scholz et al. (2016), which was based on the detection of FRB 121102 in  $T_{\text{obs}} = 36.9$  days. This is because the estimate is derived from the results of an analysis pipeline with a sensitivity different from that of the pipeline described here. Although there is some overlap between data processed by the two, data pertaining to FRB 121102 have not yet been processed by the modified pipeline. We note that our reported rate is greater than the rate derived by Scholz et al. (2016). However, the 95% confidence intervals for both have substantial overlap, implying that the detection of candidate FRB 141113 is consistent with the Scholz et al. (2016) estimate.

## 7.2. Log $N$ –Log $S$ Distribution

The observed cumulative flux density distribution of the FRB population is modeled as a power law with an index  $\alpha$  (hereafter, the log  $N$ –log  $S$  slope), such that the number of FRBs with a flux density greater than  $S$  is  $N(>S) \propto S^{-\alpha}$ . For a local, uniformly distributed, non-evolving source population,  $\alpha = 1.5$  with any deviation from this value supporting the existence of a cosmological and/or evolving source population.

Here we derive constraints on  $\alpha$  by performing simulations of cumulative flux density distributions of the FRB population. These simulations utilize results from the analysis pipeline detailed in Lazarus et al. (2015), which searched  $T_{\text{obs}} = 36.9$  days with a threshold S/N of 9.2 (hereafter, search A) and the analysis pipeline discussed in this work searching  $T_{\text{obs}} = 24$  days with a threshold S/N of 8 (hereafter, search B). Observations from these two searches are key in constraining the log  $N$ –log  $S$  slope. We include the near sidelobe detection of FRB 121102 in search A and assume, at least initially, that FRB 141113 was detected in the main beam for search B. We also account for non-detections in the main beam and near sidelobes, for searches A and B, respectively, under our initial assumption. The sensitivity threshold and sky coverage assumed for the main beam are discussed in Section 7.1, while those for the near sidelobe are calculated based on the



**Figure 11.** Predicted flux density per beam from free-free emission of a nebula at 10 kpc contributing the excess DM toward FRB 141113 seen with recent VLA B-configuration observations (orange), the VLA NVSS (green), and Parkes CHIPASS (purple). In each case, the upper and lower lines correspond to the excess DM relative to the NE2001 and YMW16 electron density models, respectively. The dashed horizontal lines indicate the observed upper limit for each survey. The solid horizontal bars indicate nebula sizes that are excluded by observation for the NE2001 (upper) and YMW16 (lower) electron density models. The shaded regions are excluded due to the requirement that the plasma be optically thin (gray) and non-detections from IPHAS H $\alpha$  point sources (blue).

corresponding values for the full FOV after subtracting the contribution of the main beam. Additionally, we account for the non-detection of any event in the far-out sidelobes for both these searches. Although the survey is sensitive to such ultra-bright off-axis bursts occurring over the visible hemisphere with a sensitivity described by Equation (19) of Deneva et al. (2009), their occurrence can likely be ruled out due to the absence of multibeam detections.

The simulations were performed by varying the log  $N$ -log  $S$  slope in the range,  $0 < \alpha \leq 2$ , in steps of 0.1. All trial values were assumed to be equally probable with thousands of runs performed for each. For each of these runs, a flux density distribution was generated, which was consistent with the low-latitude FRB rate of  $285^{+1416}_{-237}$  bursts sky $^{-1}$  day $^{-1}$  above 1 Jy, estimated by Vander Wiel et al. (2016). Based on these flux density distributions, we computed a detection rate  $R$ , in bursts sky $^{-1}$  day $^{-1}$ , above the sensitivity thresholds corresponding to the main beam, as well as the near and far-out sidelobes for both searches A and B. The number of detections for a given search and ALFA beam region for each simulation run is sampled from a Poisson distribution with a mean of  $RT_{\text{obs}}\Omega$ , where  $\Omega$  is defined in Section 7.1. A run is counted as a success if the number of simulated detections for all regions of the ALFA beam for both searches is equal to that for the observations. An additional criterion for a successful run is the flux density of the detected bursts in the simulations lying in the range of possible flux densities for the observed bursts (FRB 121102 and candidate FRB 141113).

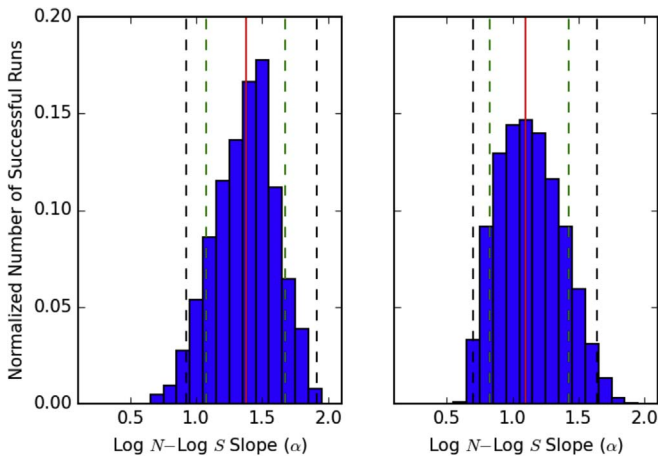
For determining flux densities of the observed bursts, we injected pulses with DM and widths equal to those of FRB 121102 and candidate FRB 141113 in PALFA pointings and obtained the range for which these pulses are detected with the same S/N as observed in the pipeline. The system flux used in this analysis varied for the two sources. The mean system flux for the main beam of 5 Jy was used for FRB 141113, as it is not possible to localize the burst position in the ALFA beam.

However, we can obtain a better estimate for the gain and hence the system flux for the position of FRB 121102, as it has been localized to milliarcsecond precision owing to its repeat bursts (Chatterjee et al. 2017). We model the ALFA beam pattern (Spitler et al. 2014) and find the gain at the position of FRB 121102 to be 0.6–0.7 K Jy $^{-1}$  (accounting for ALFA pointing errors), which we use to calculate the system flux and the observed flux density.

Based on the relative number of successful runs for each trial value of  $\alpha$ , normalized by the total number of runs and plotted in the left panel of Figure 12, we find that the detection of candidate FRB 141113 and additional PALFA observations imply a median  $\alpha$  of 1.4 with the 95% confidence interval ranging from  $0.9 < \alpha < 1.9$ . We reject  $\alpha < 0.9$  at the 95% confidence level because the implied abundance of bright bursts is inconsistent with the lack of off-axis multibeam detections with PALFA. Steeper log  $N$ -log  $S$  slopes ( $\alpha > 1.9$ ) are rejected because detection of a single faint burst is unlikely, considering the implied abundance of faint bursts in this case.

The above constraint is on the *observed* log  $N$ -log  $S$  slope, which due to propagation effects can be different from the slope intrinsic to the population. While diffractive interstellar scintillation with its small decorrelation bandwidth at low Galactic latitudes is unlikely to be important (Macquart & Johnston 2015), effects such as plasma lensing in FRB host galaxies can enhance flux densities of faint bursts (Cordes et al. 2017).

Our above reported constraints have substantial overlap with those reported for the observed log  $N$ -log  $S$  slope by Oppermann et al. (2016;  $0.8 < \alpha < 1.7$ ), Caleb et al. (2016;  $0.6 < \alpha < 1.2$ ), and Lawrence et al. (2017;  $0.57 < \alpha < 1.25$ ). However, these constraints are inconsistent with those reported by Vedantham et al. (2016;  $0.5 < \alpha < 0.9$ ), based on multiple-beam detections with Parkes surveys and other detections with telescopes of varied diameters. By running our simulations for the case of the candidate FRB 141113 being a false positive



**Figure 12.** Normalized number of MC runs for which the number and flux density of detections matched with results of FRB searches with the PALFA survey, plotted for all trial values of  $\alpha$ . While constraints on  $\alpha$  in both panels are based on the detection of FRB 121102, the left panel further assumes that FRB 141113 is astrophysical, while the right panel assumes it is a false positive. The median value for  $\alpha$  is denoted by the red, solid line with  $1\sigma$  and  $2\sigma$  confidence intervals denoted by the green and black dashed lines, respectively.

event, we find a significant shift in our constraints to a median  $\alpha$  of 1.1 with 95% bounds ranging from 0.7 to 1.6 (see the right panel of Figure 12), which has overlap with the Vedantham et al. (2016) constraints. Confirming whether the event is an FRB by observations of repeat bursts could thus have strong implications for studies of the cumulative flux density distribution of the FRB population.

Additionally, our constraints are in tension with those estimated by Bhandari et al. (2018;  $1.6 < \alpha < 3.4$ ) and Macquart & Ekers (2018;  $1.9 < \alpha < 3.9$ ), using a maximum likelihood analysis technique for FRBs detected with the Parkes telescope above the observationally complete fluence threshold of 2 Jy ms. Such steep log  $N$ -log  $S$  slopes predicting an abundance of faint bursts are already unlikely, based on the event rate implied by the discovery of FRB 121102 with the PALFA survey (Scholz et al. 2016). However, constraints based on results from the Arecibo and Parkes telescopes can be reconciled if the log  $N$ -log  $S$  slope flattens at low flux densities, in which case a single power law cannot describe the flux density distribution of the observed FRB population, as suggested by Macquart & Ekers (2018).

Our reported constraints depend strongly on our assumptions. Varying the reference FRB rate to be the all-sky estimate of  $587_{-315}^{+337}$  FRBs  $\text{sky}^{-1} \text{day}^{-1}$  above a peak flux density of 1 Jy reported by Lawrence et al. (2017) yields  $\alpha = 1.2_{-0.4}^{+0.5}$  (95% bounds). Additionally, assuming FRB 141113 to have been in the near sidelobe instead of the main beam modifies the constraint to be  $\alpha = 1.25_{-0.4}^{+0.5}$ .<sup>28</sup> Although there are factors we did not account for while calculating the range of fiducial gain values for FRB 121102 (for, e.g., rotation of the receiver at the time of observation), we find no significant change in our constraints,

<sup>28</sup> We do not consider the possibility of the candidate FRB 141113 being an off-axis detection, as it is difficult to know the fraction of the field of view for which particular ray paths into the optics of the ALFA receiver could result in a single-beam detection. Therefore, our reported constraints might not be valid if the flux density of the candidate FRB was greater than  $\sim 10^3$  Jy. However, this is unlikely considering that no bursts brighter than 9.2 KJy were detected in a search at 1.4-GHz conducted with the Bleien Radio Observatory for an observing time of 590 days (Saint-Hilaire et al. 2014).

even if the full range of gains possible for the inner edge of the sidelobe of ALFA is used ( $0.4\text{--}1.0 \text{ KJy}^{-1}$ ; Spitler et al. 2014).

## 8. Conclusion

We have described a new, more systematic single-pulse pipeline to improve the search for pulsars, RRATs, and FRBs in the PALFA survey. The pipeline adds postprocessing features to efficiently identify astrophysical single pulses.

We also performed a robust sensitivity analysis of the PALFA survey to single pulses using the injection of synthetic signals into survey data. We find that for pulse widths  $< 5$  ms, our survey is at most a factor of  $\sim 2$  less sensitive to single pulses than the theoretical predictions. For pulse widths  $> 10$  ms, as the DM decreases, the degradation in sensitivity gets worse by up to a factor of  $\sim 4.5$ . In order to better understand the actual sensitivities to single pulses in various radio transient surveys, we recommend similar characterization of their deployed detection pipelines.







Using our pipeline, we have discovered one pulsar and two RRATs that were not detected using periodicity searching techniques, six pulsars that were detected by both single pulse and periodicity pipelines, three candidate RRATs, and one candidate FRB. This latter source, FRB 141113, has a DM more than twice the likely Galactic maximum along the line of sight, and multiwavelength observations show it is very likely to be extragalactic. If so, it is consistent with being one of the lowest luminosity FRBs yet discovered. Simulations accounting for the sensitivity of PALFA and the discovery of FRB 121102 in addition to this new source indicate that the slope of the log  $N$ -log  $S$  relation for the FRB population (i.e.,  $N(>S) \propto S^{-\alpha}$ ) is  $\alpha = 1.4 \pm 0.5$  (95% confidence). The steepness of that distribution is at odds with previous suggestions of a much flatter slope (Vedantham et al. 2016). However, relaxing some reasonable assumptions in our calculation results in somewhat lower mean slopes, with uncertainty ranges that still bracket flatter population distributions.

D.A. is supported by the NSF OIA-1458952. M.B. is supported by a Mitacs Globalink Graduate Fellowship. A.B., F.C., S.C., J.M. C., S.M.R., I.H.S., M.A.M., D.R.L., W.W.Z., R.F., B.N., and K.S. are members of the NANOGrav Physics Frontiers Center, which is supported by the National Science Foundation award number 1430284. P.C. is supported by an FRQNT Doctoral Research Award and a Mitacs Globalink Graduate Fellowship. E.P. is a Vanier Scholar. VMK holds the Lorne Trottier Chair in Astrophysics and Cosmology and a Canada Research Chair, and receives support from an NSERC Discovery grant and Herzberg Award, from an R. Howard Webster Foundation Fellowship from the Canadian Institute for Advanced Research (CIFAR), and from the FRQNT Centre de Recherche en Astrophysique du Quebec. D.R.L. is supported by NSF AST-1516958 and NSF OIA-1458952. P.S. is supported by a DRAO Covington Fellowship from the National Research Council Canada. M.A.M. acknowledges support from NSF Award Number 1458952. The National Radio Astronomy Observatory is a facility of the National Science Foundation operated under cooperative agreement by Associated Universities, Inc. S.M.R. is a CIFAR Senior Fellow. R.S.W. acknowledges financial support by the European Research Council (ERC) for the ERC Synergy grant BlackHoleCam under contract no. 610058. W.W.Z. is supported by the CAS Pioneer Hundred Talents Program, National Key R&D Program of China No. 2017YFA0402600, and National Nature Science Foundation of



China No. 11743002. K.C.V. acknowledges the following ARCC students who have contributed to observations: Brent Cole, Keith Bohler, and Yhamil Garcia. J.S.D. is supported by the NASA Fermi program. P.C.C.F. gratefully acknowledges financial support by the European Research Council for the Starting grant BEACON under contract No. 279702, and continued support from the Max Planck Society. J.W.T.H. acknowledges funding from an NWO Vidi fellowship and from the European Research Council under the European Union's Seventh Framework Programme (FP/2007-2013)/ERC Starting grant agreement No. 337062 ("DRAGNET"). Pulsar research at UBC is supported by an NSERC Discovery grant and by CIFAR. The research leading to these results has received funding from the European Research Council under the European Union's Seventh Framework Programme (FP/2007-2013)/ERC grant Agreement No. 617199. The Arecibo Observatory is operated by SRI International under a cooperative agreement with the National Science Foundation (AST-1100968), and in alliance with Ana G.Méndez-Universidad Metropolitana, and the Universities Space Research Association. The CyberSKA project was funded by a CANARIE NEP-2 grant. Computations were made on the supercomputer Guillimin at McGill University, managed by Calcul Québec and Compute Canada. The operation of this supercomputer is funded by the Canada Foundation for Innovation (CFI), NanoQuébec, RMGA, and the Fonds de recherche du Québec—Nature et technologies (FRQNT).

### ORCID iDs

M. Bhardwaj  <https://orcid.org/0000-0002-3615-3514>  
 S. Chatterjee  <https://orcid.org/0000-0002-2878-1502>  
 P. Chawla  <https://orcid.org/0000-0002-3426-7606>  
 V. M. Kaspi  <https://orcid.org/0000-0001-9345-0307>  
 D. R. Lorimer  <https://orcid.org/0000-0003-1301-966X>  
 M. A. McLaughlin  <https://orcid.org/0000-0001-7697-7422>  
 E. Parent  <https://orcid.org/0000-0002-0430-6504>  
 Z. Pleunis  <https://orcid.org/0000-0002-4795-697X>  
 S. M. Ransom  <https://orcid.org/0000-0001-5799-9714>  
 P. Scholz  <https://orcid.org/0000-0002-7374-7119>  
 R. S. Wharton  <https://orcid.org/0000-0002-7416-5209>  
 W. W. Zhu  <https://orcid.org/0000-0001-5105-4058>  
 F. Camilo  <https://orcid.org/0000-0002-1873-3718>  
 J. M. Cordes  <https://orcid.org/0000-0002-4049-1882>  
 F. Crawford  <https://orcid.org/0000-0002-2578-0360>  
 J. S. Deneva  <https://orcid.org/0000-0003-1226-0793>  
 R. D. Ferdman  <https://orcid.org/0000-0002-2223-1235>  
 P. C. C. Freire  <https://orcid.org/0000-0003-1307-9435>  
 I. Stairs  <https://orcid.org/0000-0001-9784-8670>  
 K. Stovall  <https://orcid.org/0000-0002-7261-594X>

### References

Anderson, L. D., Bania, T., Balsler, D. S., et al. 2014, *ApJS*, 212, 1  
 Barentsen, G., Farnhill, H. J., Drew, J. E., et al. 2014, *MNRAS*, 444, 3230

Bates, S. D., Lorimer, D. R., Rane, A., & Swiggum, J. 2014, *MNRAS*, 439, 2893  
 Bhandari, S., Keane, E. F., Barr, E. D., et al. 2018, *MNRAS*, 475, 1427  
 Burke-Spolaor, S., & Bailes, M. 2010, *MNRAS*, 402, 855  
 Burke-Spolaor, S., Bailes, M., Johnston, S., et al. 2011, *MNRAS*, 416, 2465  
 Calabretta, M. R., Staveley-Smith, L., & Barnes, D. G. 2014, *PASA*, 31, e007  
 Caleb, M., Flynn, C., Bailes, M., et al. 2016, *MNRAS*, 458, 718  
 Carpenter, J. M., Snell, R. L., & Schloerb, F. P. 1995, *ApJ*, 445, 246  
 Chatterjee, S., Law, C. J., Wharton, R. S., et al. 2017, *Natur*, 541, 58  
 Chavarría, L. A., Allen, L. E., Hora, J. L., et al. 2008, *ApJ*, 682, 445  
 Condon, J. J., Cotton, W. D., Greisen, E. W., et al. 1998, *AJ*, 115, 1693  
 Cordes, J. M., Freire, P. C. C., Lorimer, D. R., et al. 2006, *ApJ*, 637, 446  
 Cordes, J. M., & Lazio, T. J. W. 2003, arXiv:astro-ph/0301598  
 Cordes, J. M., & McLaughlin, M. A. 2003, *ApJ*, 596, 1142  
 Cordes, J. M., Wasserman, I., Hessels, J. W. T., et al. 2017, *ApJ*, 842, 35  
 Deneva, J. S., Cordes, J. M., McLaughlin, M. A., et al. 2009, *ApJ*, 703, 2259  
 Draper, P. W., Scarrott, S. M., & Tadhunter, C. N. 1993, *MNRAS*, 262, 1029  
 Drew, J. E., Greimel, R., Irwin, M. J., et al. 2005, *MNRAS*, 362, 753  
 Eatough, R. P., Keane, E. F., & Lyne, A. G. 2009, *MNRAS*, 395, 410  
 Edwards, R. T., Bailes, M., van Straten, W., & Britton, M. C. 2001, *MNRAS*, 326, 358  
 Inoue, S. 2004, *MNRAS*, 348, 999  
 Ioka, K. 2003, *ApJL*, 598, L79  
 Jacoby, B. A., Bailes, M., Ord, S. M., Edwards, R. T., & Kulkarni, S. R. 2009, *ApJ*, 699, 2009  
 Karako-Argaman, C., Kaspi, V. M., Lynch, R. S., et al. 2015, *ApJ*, 809, 67  
 Keane, E. F., Kramer, M., Lyne, A. G., Stappers, B. W., & McLaughlin, M. A. 2011, *MNRAS*, 415, 3065  
 Keith, M. J., Jameson, A., van Straten, W., et al. 2010, *MNRAS*, 409, 619  
 Kiddle, C., Andrecut, M., Brazier, A., et al. 2011, in ASP Conf. Ser. 442, *Astronomical Data Analysis Software and Systems XX*, ed. I. N. Evans et al. (San Francisco, CA: ASP), 669  
 Kondratiev, V. I., McLaughlin, M. A., Lorimer, D. R., et al. 2009, *ApJ*, 702, 692  
 Kulkarni, S. R., Ofek, E. O., & Neill, J. D. 2015, arXiv:1511.09137  
 Kulkarni, S. R., Ofek, E. O., Neill, J. D., Zheng, Z., & Juric, M. 2014, *ApJ*, 797, 70  
 Lawrence, E., Vander Wiel, S., Law, C., Burke Spolaor, S., & Bower, G. C. 2017, *AJ*, 154, 117  
 Lazarus, P., Brazier, A., Hessels, J. W. T., et al. 2015, *ApJ*, 812, 81  
 Lorimer, D. R., Bailes, M., McLaughlin, M. A., Narkevic, D. J., & Crawford, F. 2007, *Sci*, 318, 777  
 Lorimer, D. R., Faulkner, A. J., Lyne, A. G., et al. 2006, *MNRAS*, 372, 777  
 Lorimer, D. R., & Kramer, M. 2005, *Handbook of Pulsar Astronomy* (Cambridge: Cambridge Univ. Press)  
 Macquart, J. P., & Ekers, R. D. 2018, *MNRAS*, 474, 1900  
 Macquart, J.-P., & Johnston, S. 2015, *MNRAS*, 451, 3278  
 Manchester, R. N., Lyne, A. G., Camilo, F., et al. 2001, *MNRAS*, 328, 17  
 McLaughlin, M. A., Lyne, A. G., Lorimer, D. R., et al. 2006, *Natur*, 439, 817  
 Oppermann, N., Connor, L. D., & Pen, U.-L. 2016, *MNRAS*, 461, 984  
 Parent, E., Kaspi, V. M., Ransom, S. M., et al. 2018, *ApJ*, 861, 44  
 Ransom, S. M. 2001, PhD thesis, Harvard Univ.  
 Saint-Hilaire, P., Benz, A. O., & Monstein, C. 2014, *ApJ*, 795, 19  
 Scholz, P., Spitler, L. G., Hessels, J. W. T., et al. 2016, *ApJ*, 833, 177  
 Spitler, L. G., Cordes, J. M., Hessels, J. W. T., et al. 2014, *ApJ*, 790, 101  
 Spitler, L. G., Scholz, P., Hessels, J. W. T., et al. 2016, *Natur*, 531, 202  
 Vander Wiel, S., Burke-Spolaor, S., Lawrence, E., Law, C. J., & Bower, G. C. 2016, arXiv:1612.00896  
 Vedantham, H. K., Ravi, V., Mooley, K., et al. 2016, *ApJL*, 824, L9  
 Wright, E. L., Eisenhardt, P. R. M., Mainzer, A. K., et al. 2010, *AJ*, 140, 1868  
 Yao, J. M., Manchester, R. N., & Wang, N. 2017, *ApJ*, 835, 29  
 Zhu, W. W., Berndsen, A., Madsen, E. C., et al. 2014, *ApJ*, 781, 117